BRNO UNIVERSITY OF TECHNOLOGY

VYSOKÉ UČENÍ TECHNICKÉ V BRNĚ

CENTRAL EUROPEAN INSTITUTE OF TECHNOLOGY BUT

STŘEDOEVROPSKÝ TECHNOLOGICKÝ INSTITUT VUT

STATIC AND DYNAMIC PROPERTIES OF NANOSTRUCTURED MAGNETIC MATERIALS

STATICKÉ A DYNAMICKÉ VLASTNOSTI NANOSTRUKTUROVANÝCH MAGNETICKÝCH MATERIÁLŮ

DOCTORAL THESIS SUMMARY

TEZE DIZERTAČNÍ PRÁCE

AUTHOR
AUTOR PRÁCE

Ing. Marek Vaňatka

SUPERVISOR
ŠKOLITEL

Ing. Michal Urbánek, Ph.D.

BRNO 2020

Contents

Introduction

The discovery of various forms of magnetoresistance led to massive development in magnetic recording technologies during the 1990s, increasing the storage capacity and shrinking the size dramatically. This gave rise to the new discipline in magnetism called spintronics – a field of electronics considering the spin of an electron as an additional physical degree of freedom, which can be manipulated to obtain unique functionalities given solely by the magnetic origin of the spintronic system [1]. The spin-dependent phenomena in spintronic devices rely on the spin ordering described by micromagnetism. This theory explains, e.g., the formation of domains and various spin structures [2], which is discussed at the beginning of Chapter 1.

One of the systems studied by numerous scientists, including our research group, is the magnetic vortex in micron-sized disks patterned from soft magnetic materials [3]. Magnetic vortices consist of a magnetization curling in the disk's plane around a vortex core located at the center of the disk, where the magnetization points perpendicular to that plane [2,4,5]. This work studies the magnetic vortex nucleation upon the field decrease from saturation, which is dealt with in Chapter 3. We will show that the magnetization evolution between the fully saturated state and the fully nucleated vortex proceeds via different spin configurations called the nucleation states. The nucleation states are described and classified using several probing techniques presented in Chapter 2, e.g., transmission electron microscopy and electrical detection via anisotropic magnetoresistance.

Magnetic vortices have also been reported to function as spin-wave emitters [6], and spin-waves deserve high interest due to their potential in computing [7] alongside spintronics. One of the exciting characteristics is that they do not move electric charges (like electric waves) and therefore lack the associated energy dissipation in the form of Joule heating. They also have short wavelengths (micro- to nanometer) and high (up to THz [8]) frequency range. Spin-wave propagation can be probed in an experiment called the propagating spin-wave spectroscopy (PSWS), which is purely enabled by a VNA [9]. It uses a pair of microwave antennas to excite and detect the spin-waves, where the VNA records the spin-wave magnitude and phase. Multiple aspects of the PSWS experimental method will be presented in the last section of Chapter 4.

An essential characteristic of spin-waves is the dispersion relation, which connects the wavelength (in terms of the k-vector) of the spin-wave to its frequency. It is not easy to measure a dispersion in detail, which would typically be done using phase-resolved BLS. This is very time consuming and therefore allows only for several points, while in Chapter 5, we present a relatively fast VNA-based all-electrical approach providing hundreds of measurement points in the dispersion.

Lastly, Chapter 6 will introduce a concept of freestanding antennas, where we attempted to transfer the spin-wave excitation element away from the sample. Our innovative approach allows for skipping the fabrication step of the excitation antennas on each sample and using a positionable device instead, allowing for much more rapid experimental flow.

1 Introduction on micromagnetic states and spin dynamics

1.1 Basic relations in micromagnetism

The field of micromagnetism studies magnetic matter from the mesoscopic point of view: it does not study the interaction of every pair of spins of which the magnetic material consists, but it is a continuous theory. The first vital quantity to be introduced is magnetization, defined as the density of magnetic moments $\boldsymbol{\mu}$:

$$\boldsymbol{M} = \frac{\mathrm{d}\boldsymbol{\mu}}{\mathrm{d}V}, \tag{1.1}$$

while it is understood as a continuous function of position in space. The maximum value of magnetization is called the saturation magnetization M_s and it takes place when all of the moments are aligned parallel. For later use, we will also define a normalized magnetization vector $\boldsymbol{m}$:

$$\boldsymbol{m} = \frac{\boldsymbol{M}}{M_\mathrm{S}}. \tag{1.2}$$

1.2 Micromagnetic energies

The magnetic states, i.e., the configurations of spins formed in mesoscopic structures, are not random but result from competing magnetic interactions. There are four fundamental interactions present between individual magnetic spins. In the micromagnetic framework, we can represent them with their energy terms.

The interactions are then summarized into the total micromagnetic energy, where the final magnetization state is the result of minimizing it; a stable magnetic state reflects either a local or an absolute energy minimum [10,11]. The total energy is the sum of the four parts:

$$E_\mathrm{tot} = E_\mathrm{ex} + E_\mathrm{d} + E_\mathrm{Z} + E_\mathrm{a}. \tag{1.3}$$

1.2.1 Energy components

The first component of the total energy E_tot is the exchange energy E_ex, associated with the exchange interaction, which enables the existence of ferromagnetism and is purely of the quantum mechanical origin [10,11]. Its basic consequence is that the adjacent magnetic moments prefer to be aligned collinearly. Its value is then calculated as the volume integral:

$$E_\mathrm{ex} = \iiint A_\mathrm{ex}\left[(\nabla m_x)^2 + \left(\nabla m_y\right)^2 + (\nabla m_z)^2\right]\mathrm{d}V, \tag{1.4}$$

where A_ex is called the exchange stiffness constant in units of J/m. Exchange is a short distance interaction, where the quantity describing the length within which the exchange interaction is dominant is called the exchange length:

$$l_\mathrm{ex} = \sqrt{\frac{2A_\mathrm{ex}}{\mu_0 M_\mathrm{S}^2}}. \tag{1.5}$$

Contrary to the exchange interaction, the dipolar energy E_d prefers two adjacent spins to align in the opposite direction, and it affects the spins at a more extended scale than exchange. It can be calculated using the H-field inside the material (the demagnetizing field):

$$E_{\mathrm{d}} = -\frac{1}{2}\mu_0 \iiint \boldsymbol{M} \cdot \boldsymbol{H}_{\mathrm{d}}\, \mathrm{d}V, \tag{1.6}$$

where the demagnetizing field $\boldsymbol{H}_d$ opposes the magnetization direction. Minimizing the dipolar energy reduces the volume and surface magnetic charges, which is called the charge avoidance principle. The sample shape plays a crucial role here because the dipolar energy is influenced by the sample's geometry and can create preferred axes of the magnetization orientation. This effect is often referred to as the shape anisotropy [10].

The energy describing the interaction of the magnetization with external magnetic fields is called Zeeman energy E_{Z}. The Zeeman energy represents the energetical penalty for spins not pointing in the external field's ($\boldsymbol{H}_{\mathrm{ext}}$) direction, where it is calculated similarly as the previous dipolar energy:

$$E_{\mathrm{Z}} = -\mu_0 \iiint \boldsymbol{M} \cdot \boldsymbol{H}_{\mathrm{ext}}\, \mathrm{d}V. \tag{1.7}$$

The last energy term considers the crystal (electronic) structure of magnetic material, where the magnetization aligns preferentially along specific crystallographic directions called easy axes. The associated energy of anisotropy can again be calculated in the form of a volume integral. In the simplest case of the uniaxial anisotropy, having only one easy axis, which is found in hexagonal or orthorhombic crystals, the energy term is

$$E_{\mathrm{a}} = \iiint K_{\mathrm{u}} \sin\theta\, \mathrm{d}V, \tag{1.8}$$

where K_{u} is the energy density of the uniaxial anisotropy, and θ is the angle between the easy axis and the vector of magnetization $\boldsymbol{M}$.

1.2.2 Formation of domains and spin structures

The spin structure of magnetic materials in bulk or layers is often broken into domains. This results from competing micromagnetic energies with the total energy E_{tot} being at its minimum when a stable state is reached. Two of the energies, Zeeman energy and anisotropy energy, favor spin alignment along a specific direction given by the effective magnetic field (discussed later) and the easy anisotropy axis respectively. When one of them is dominant, we can expect most of the spins to be aligned with the preferred direction. Those two energies can also be controlled externally. Zeeman energy is given by the external magnetic field, which can be eliminated, and anisotropy can be suppressed by preparing the materials in a way that the magnetic anisotropy strength is negligible, e.g., polycrystalline NiFe or amorphous CoFeB.

On the other hand, exchange and dipolar energies are intrinsic and thus are always present. We will use the illustration in Fig. 1.1 to provide an insight into the energy influence on a micron-sized magnetic square structure. (a) shows the resulting spin pattern for the case that we could turn off all of the energy contributions except for the exchange interaction. This interaction favors the spins to be aligned parallel. Therefore, the whole sample consists of a single magnetic domain. Fig. 1.1(b) shows the result of energy competition after introducing the dipolar energy to the system. The dipolar energy favors curling of the spins. This is the opposite to exchange, but it acts at long distances, while the characteristic reach of the exchange interaction is very short and is given by the exchange length l_{ex}. The result then exhibits a magnetic flux closure – a typical feature in the minimization of dipolar energy. The flux closing patterns minimize the surface charges following the charge avoidance principle [10]. This pattern in a magnetic square was first predicted by Landau, and is called the Landau pattern [2]. It consists of four domains with their magnetization circulating around the center point, known as the core, in which the magnetization points out-of-plane. The curling nature of magnetization in this pattern with a core in the middle is what essentially makes it a

magnetic vortex. Fig. 1.1(c,d) illustrates the addition of Zeeman energy and anisotropy energy, where the spin alignment will be influenced by the external magnetic field and the easy axis caused by anisotropy. The magnetic vortex can still exist, but in Fig. 1.1(b), it will be deformed to reflect the added energy terms.

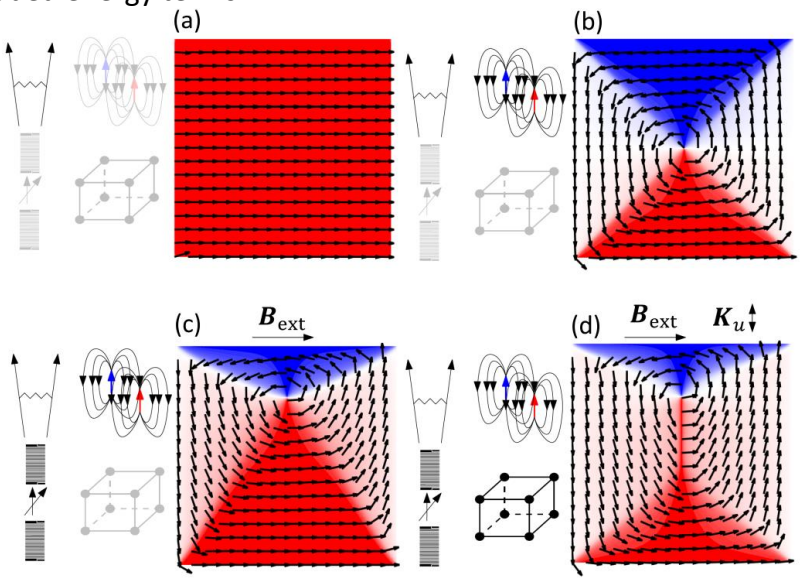

Fig. 1.1: Influence of added energy contributions. (a) Exchange energy only. (b) Competing exchange and dipolar energies lead to the formation of a flux-closing Landau pattern. (c) Added Zeeman energy in the form of the external magnetic field energetically favors the spins oriented along the external magnetic field direction. (d) Bidirectional anisotropy term tries to align the moments to the easy axis. The final spin structure is a result of all four components in competition. Reprinted from [12].

1.3 Magnetic vortices in thin magnetic disks

Now, if we consider a cylindrical geometry with the diameter D of the cylinder much larger than the thickness t (we will call it a disk for simplicity), the magnetic spins will follow the same logic as in the previous section. The ground state will almost always be the magnetic vortex exhibiting the spins' characteristic flux-closing circular pattern. Only now the four domains will not be formed because the disk has rotational symmetry. Instead, continuous circulation of spins around an out-of-plane core will take place. The exceptions to the vortex creation are disks either too small (both D and t well under 100 nm), in which case the structure will be in a single domain state [13], or too large with respect to the thickness (e.g., $D > 10$ μm and t~10 nm), which will result in a multidomain state.

The symmetry of a disk provides four energetically equal (degenerate) vortex states. They can be described by two independent parameters: circulation and polarity. The circulation is defined by the sense of the in-plane magnetization curling (clockwise, $c = -1$ or counterclockwise, $c = 1$) while the out-of-plane magnetization direction gives the polarity in the vortex core (pointing up, $p = 1$ or down, $p = -1$).

1.3.1 Magnetization dynamics

Even though we have already established that the magnetic configuration will correspond to a minimum of the total energy, we have not described how the minimum is reached. The answer is that magnetic moments will follow an equation of motion which describes a damped precession of each spin to the direction of the local effective magnetic field $\boldsymbol{H}_{\text{eff}}$, calculated from the above mentioned micromagnetic energies as:

$$\boldsymbol{H}_{\text{eff}} = -\frac{1}{\mu_0}\frac{\partial E_{\text{tot}}}{\partial \boldsymbol{M}}. \tag{1.9}$$

The equation of motion is then called the Landau-Lifshitz-Gilbert (LLG) equation [14–16]:

$$\frac{\mathrm{d}\boldsymbol{M}}{\mathrm{d}t} = -\gamma \boldsymbol{M} \times \boldsymbol{H}_{\text{eff}} + \frac{\alpha}{M_s}\boldsymbol{M} \times \frac{\mathrm{d}\boldsymbol{M}}{\mathrm{d}t}, \tag{1.10}$$

where γ is the gyromagnetic ratio. The right part consists of two contributors: the first part is the precessional term and the second part represents the damping term. The precessional term describes the spin's motion in an ideal case of a system with zero damping. As every real system has nonzero damping, this needs to be taken into account by the second term proportional to the damping parameter α. The damping term causes the magnetic moment to follow a spiral path until it is aligned to the direction of the effective field $\boldsymbol{H}_{\text{eff}}$ by following a spiral.

1.4 Ferromagnetic resonance (FMR)

One important solution of the LLG equation (1.10) is called the ferromagnetic resonance (FMR). It is a spatially uniform collective oscillation. The resonant (thickness independent) frequency of a thin film can be calculated from the Kittel formula [17]:

$$f_{\text{FMR}} = \frac{\gamma}{2\pi}\sqrt{B(B + \mu_0 M_S)}, \tag{1.11}$$

where γ is the gyromagnetic ratio, and B is the effective magnetic field where it should be understood as the sum of the external magnetic field B_{ext} with other contributions, e.g., from anisotropy. Because the external magnetic field B_{ext} is the control parameter of the experiment, we will rewrite the equation for $B = B_{\text{ext}} + B_0$ where B_0 will sum all other effective field contributions:

$$f_{\text{FMR}} = \frac{\gamma}{2\pi}\sqrt{(B_{\text{ext}} + B_0)(B_{\text{ext}} + B_0 + \mu_0 M_S)}. \tag{1.12}$$

In the case of uniaxial anisotropy, $B_0 = \mu_0 H_{\text{an}}$, and can be calculated as

$$H_{\text{an}} = \frac{2K_u}{M_s}\sin\theta, \tag{1.13}$$

where K_u is the energy density of uniaxial anisotropy, and θ is the angle between the magnetization and the direction of the easy axis. The anisotropy field may be obtained using an angle-dependent FMR experiment but note that it may be difficult to distinguish between the B_0 field contributors. Examples of FMR frequency calculations are shown in Fig. 1.2.

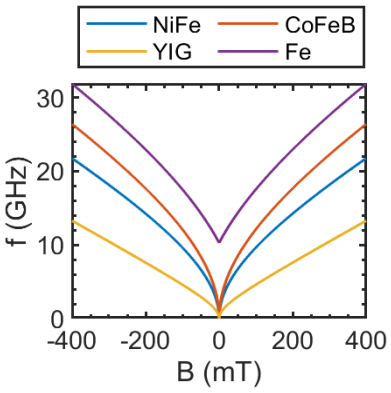

Fig. 1.2: Calculated FMR of materials used in this work: NiFe ($M_s = 800$ kA/m, $\gamma/2\pi = 29$ GHz/T, $B_0 = 0$ mT), CoFeB ($M_s = 1.2$ MA/m, $\gamma/2\pi = 30.2$ GHz/T, $B_0 = 0$ mT), YIG ($M_s = 142$ kA/m, $\gamma/2\pi = 27.6$ GHz/T, $B_0 = 0$ mT), and epitaxial Fe ($M_s = 1.74$ MA/m, $\gamma/2\pi = 29$ GHz/T, $B_0 = 56$ mT) in easy axis.

1.5 Perpendicular standing spin-waves (PSSW)

The perpendicular standing spin-waves (PSSW) are exchange dominated, quantized modes in thin magnetic layers of thickness t. The order of this quantization can be described by the integer parameter n. Their frequency is then described by the Herring-Kittel formula [18]:

$$f_{\mathrm{PSSW}} = \frac{\gamma}{2\pi}\sqrt{\left(B + \frac{2A_{\mathrm{ex}}}{M_S}\left(\frac{n\pi}{t}\right)^2\right)\left(B + \frac{2A_{\mathrm{ex}}}{M_S}\left(\frac{n\pi}{t}\right)^2 + \mu_0 M_S\right)}. \tag{1.14}$$

For $n = 0$, the equation reduces to the Kittel formula (1.11) and calculates the thickness independent FMR. Fig. 1.3 shows example calculations for modes up $n = 3$.

A spin-wave can be confined in the layer along the out-of-plane direction and propagate along the layer's in-plane direction at the same time. The previous equation will not suffice to describe the confined propagating modes, and a more general model, provided in the following Section 1.7, will be necessary.

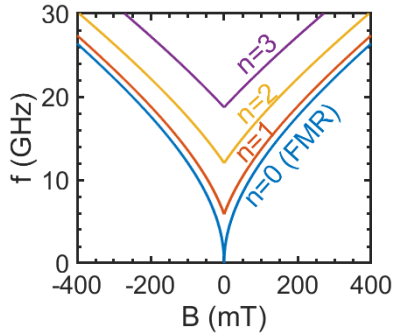

Fig. 1.3: Calculated PSSW modes using the Herring-Kittel equation for CoFeB 100 nm layer: $M_s = 1.2$ MA/m, $\gamma/2\pi = 30.2$ GHz/T, $A_{ex} = 15$ pJ/m, $t = 100$ nm.

1.6 Basic modes of propagating spin-waves

Opposite to the collectively oscillating spins in the FMR experiment, it is possible to create an excitation propagating through space in the form of a wave. The length in space over which the spin-wave changes its phase by 2π is called the wavelength λ, using which we can define the k-vector (wave number) as a vector pointing in the direction of propagation and having the size

$$|\boldsymbol{k}| = \frac{2\pi}{\lambda}. \tag{1.15}$$

The k-vector has the unit rad/m, which we emphasize because some works omit to state the radians explicitly, confusing whether the radians are only not stated (as in SI units it is 1) or if there is the factor 2π difference. The k-vectors presented in this work will always be stated in units of rad/µm.

The coupling between the spins enables spin-waves' existence due to its two types: the dipolar interaction and the exchange interaction. The following subsections describe the basic modes of propagating spin-waves and their dispersion relations, covering the dipolar interaction dominated regime of propagation parallel and perpendicular to the magnetization. Although they do not consider the exchange interaction, they will provide a good and simple approximation for small k-vectors, while medium to high k-vectors, where the exchange interaction has increasing influence, will require a more thorough description that will be provided in Section 1.7. The spin-wave's group velocity and propagation length can be calculated from the dispersion relation.

1.6.1 Magnetostatic surface waves (MSSW)

When $\boldsymbol{k}$ and $\boldsymbol{M}$ are both in-plane and $\boldsymbol{k} \perp \boldsymbol{M}$, then the propagation mode is called the magnetostatic surface waves (MSSW). It was first derived by Damon and Eshbach, and therefore, it is also known as the Damon-Eshbach (DE) waves [19]. The dispersion can be calculated as follows:

$$f_{\mathrm{DE}} = \frac{\gamma}{2\pi}\sqrt{B(B+\mu_0 M_S) + \frac{(\mu_0 M_S)^2}{4}(1-e^{-2kt})}. \tag{1.16}$$

The DE mode is localized on one of the layer surfaces, and exhibits an exponential decay of the dynamic magnetization through the layer thickness. The localization shifts to the other surface upon the propagation direction reversal, which means that the DE mode is non-reciprocal [20,21].

1.6.2 Backward volume waves (BVMSW)

When $\boldsymbol{k}$ and $\boldsymbol{M}$ are again both in-plane and $\boldsymbol{k} \parallel \boldsymbol{M}$, then the propagation mode is called the backward volume magnetostatic waves (BVMSW) or simply the backward volume (BV) waves. As the name suggests, the waves propagate through the layer's volume, unlike the surface localized MSSW. The dispersion is calculated as follows:

$$f_{\mathrm{BV}} = \frac{\gamma}{2\pi}\sqrt{B\left[B+\mu_0 M_S\left(\frac{1-e^{-2kt}}{kt}\right)\right]}. \tag{1.17}$$

The BV mode exhibits a decreasing frequency in the dispersion, causing the group velocity to have the opposite sign to the phase velocity (antiparallel to the k-vector), thus the name backward waves. A comparison of the MSSW and BVMSW modes is shown in Fig. 1.4 for CoFeB parameters.

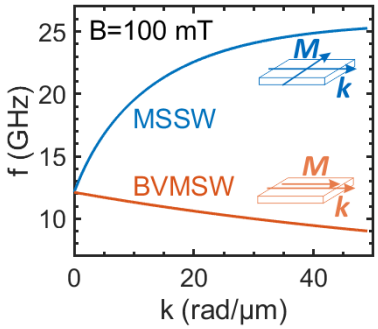

Fig. 1.4: Comparison of the spin-wave dispersion spectra of MSSW and BVMSW modes for a 30 nm CoFeB layer. ($M_S = 1.2$ MA/m, $\gamma/2\pi = 30.2$ GHz/T, $t = 30$ nm)

1.7 General description of spin-waves by Kalinikos and Slavin

The main limitation of the spin-wave modes presented in Sections 1.6.1 and 1.6.2 is the absence of the exchange interaction; the magnetic interactions were assumed to be dipolar only. The following description takes the exchange interaction into account. Hence it will be referred to as the dipole-exchange model. It will also overcome other limitations of previous expressions, which described only the cases when the k-vector is either parallel or perpendicular to magnetization, and they did not take into account the quantized modes $n > 0$ (PSSW). The dipole-exchange model presented in this section will express the dispersion relation for any angle of propagation, any quantization number (it includes PSSW as the quantized modes can also propagate, i.e., they can have a non-zero in-plane k-vector), it will also allow the use of partially pinned boundary conditions, and lastly, it will allow us to calculate mode hybridizations.

Please note that throughout this work, the symbol k (with no index) will correspond only to the absolute value of the in-plane component of the total k-vector k_{tot} [k_{tot} contains all components, as shown later in Eq. (1.22)]. The quantized part of k_{tot} is sometimes annotated κ and for the most used boundary condition of totally unpinned surface spins, it can be calculated as $\kappa_n = n\pi/t$, where n is the quantization factor. Quantization can also occur for in-plane confined elements (e.g., magnonic waveguides), which is not dealt with in this thesis (see, e.g., [12,22]).

1.7.1 Dipole-exchange dispersion relations of spin-waves

The approximative general description of spin-wave dispersions was provided in the 1980s by Kalinikos and Slavin [23], and is described with the following equations:

$$f = \frac{1}{2\pi}\sqrt{(\omega_B + A\omega_M k_{\mathrm{tot}}^2)(\omega_B + A\omega_M k_{\mathrm{tot}}^2 + \omega_M F_n)}, \tag{1.18}$$

where we can substitute:

$$\omega_B = \gamma B, \tag{1.19}$$

$$\omega_M = \mu_0 \gamma M_s, \tag{1.20}$$

$$A = l_{\mathrm{ex}}^2 = \frac{2A_{\mathrm{ex}}}{\mu_0 M_s^2}, \tag{1.21}$$

and k_{tot} is the total k-vector considering both continuous and quantized wave components:

$$k_{\mathrm{tot}} = \sqrt{k^2 + \kappa_n^2}, \tag{1.22}$$

$$\kappa_n = \frac{n\pi}{t}. \tag{1.23}$$

The number $n = 0,1,2,\ldots$ is the quantization factor for perpendicular standing spin-wave (PSSW) modes, and t is the film thickness. The factor F_n represents the following expression:

$$F_n = P_n + \sin^2\vartheta\left(1 - P_n(1+\cos^2\varphi) + \frac{\omega_M P_n(1-P_n)\sin^2\varphi}{\omega_B + A\omega_M k_{\mathrm{tot}}^2}\right), \tag{1.24}$$

where $\varphi = \angle(\boldsymbol{k}, \boldsymbol{M}_{\parallel})$ is the in-plane angle of propagation, $\varphi = 90°$ for the $\boldsymbol{k} \perp \boldsymbol{M}$ geometry and $\varphi = 0°$ for the $\boldsymbol{k} \parallel \boldsymbol{M}$ geometry. The angle ϑ is the out-of-plane angle, $\vartheta = 90°$ for in-plane magnetization and $\vartheta = 0°$ for out-of-plane magnetization.

The factor P_n depends on the surface pinning, which will be discussed later. At the extremes, P_n can be calculated for either totally unpinned or totally pinned surface spins.

$\boldsymbol{P_n}$ for totally <u>unpinned</u> surface spins ($\boldsymbol{n = 0, 1, 2, \ldots}$):

$$P_n = \frac{k^2}{k_{\mathrm{tot}}^2} - \frac{1}{1+\delta_{0n}}\frac{k^4}{k_{\mathrm{tot}}^4}\frac{2}{kt}(1-(-1)^n e^{-kt}), \tag{1.25}$$

where δ is the Kronecker delta. In this case $\delta_{0n} = 1$ for $n = 0$, and $\delta_{0n} = 0$ for $n \neq 0$.

$\boldsymbol{P_n}$ for totally <u>pinned</u> surface spins ($\boldsymbol{n = 1, 2, 3, \ldots}$):

$$P_n = \frac{k^2}{k_{\mathrm{tot}}^2} + \frac{k^2\kappa_n^2}{k_{\mathrm{tot}}^4}\frac{2}{kt}(1-(-1)^n e^{-kt}). \tag{1.26}$$

Fig. 1.5 shows representative plots of the dipole-exchange model calculated for a CoFeB layer. Fig. 1.5(a) compares the data plotted in Fig. 1.4 with the Kalinikos-Slavin model showing

the difference at higher k-vector values as this is the exchange dominated region in the dispersion. The $\boldsymbol{k} \parallel \boldsymbol{M}$ geometry now exhibits a nonmonotonic behavior with one minimum because the dispersion in the exchange dominated regime always has a rising character. Fig. 1.5(b) shows the same plot for a higher layer thickness of $t = 100$ nm, where we can observe few attributes. The $\boldsymbol{k} \perp \boldsymbol{M}$ geometry has a minimum as well as the $\boldsymbol{k} \parallel \boldsymbol{M}$ geometry, where the minimum is significantly deeper and at a higher k value. The initial slope of the $\boldsymbol{k} \perp \boldsymbol{M}$ geometry dispersion is also much steeper.

Although we plotted the spectra up to $k = 150$ rad/µm, we have to keep in mind that most experiments are limited to work only up to a few tens of rad/µm at most. The experiments presented in this work mostly did not overcome 10 rad/µm.

An interesting feature is the mode crossing of $n = 0$ mode with $n > 0$ modes, which is observable at higher thicknesses. Fig. 1.5(a) shows plots of CoFeB 100 nm layer for modes from $n = 0$ to $n = 3$, where we can see the crossings. This can potentially lead to mode hybridization as the degenerate states are prohibited, which will be discussed in the following subsection. In Fig. 1.5(b), we can also notice the minimum in the $\boldsymbol{k} \perp \boldsymbol{M}$ dispersion at approx. 50 rad/µm. This would mean that the group velocity will become negative. This was previously shown to be an inaccuracy of this model, and it is not physically valid [24].

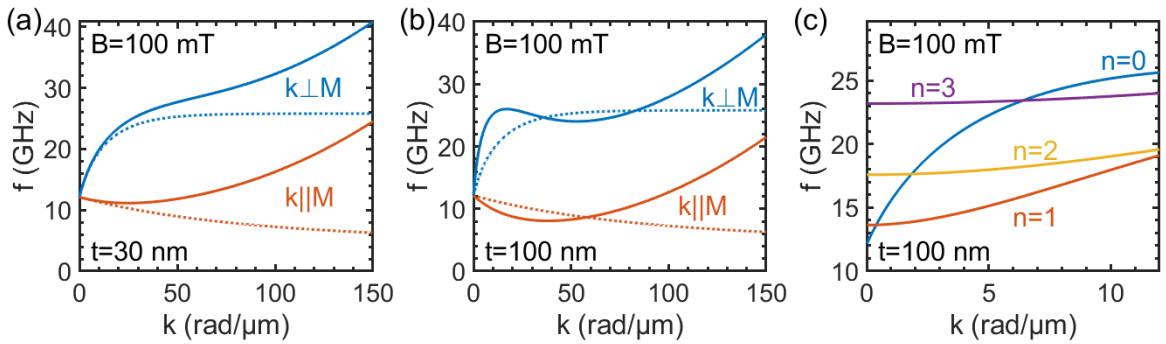

Fig. 1.5: Kalinikos-Slavin dipole-exchange model (for totally unpinned surface spins) plotted for CoFeB layer with parameters: $M_s = 1.2$ MA/m, $\gamma/2\pi = 30.2$ GHz/T, $A_{ex} = 15$ pJ/m, and thickness (a) $t = 30$ nm, (c,d) $t = 100$ nm. Dotted lines represent the dipolar-only dispersions calculated by Eq. (1.16) and (1.17). (a,b) shows the zeroth mode only, (c) shows the zeroth and the first three PSSW modes.

2 Used experimental methods with examples

2.1 Lorentz Transmission Electron Microscopy (LTEM)

Before describing the principles of magnetic imaging function in TEM, we must discuss the optics used in these microscopes. They can use either an electric or magnetic field to focus or transform the electron beam. Much lower aberrations of the magnetic type of lenses give them superiority over electrostatic lenses, and they are used almost exclusively. Furthermore, the most important lens in the microscope – the objective lens – is always the immersion type, i.e., there is a strong leak of its magnetic field to the sample space. From here originates the evident conflict of the objective's magnetic field (typical values over 2 T) with the studied

samples because the field is high enough to saturate the vast majority of the magnetic specimen. This problem is solved by equipping the microscope with an extra lens taking over the objective's purpose and by turning the objective lens off. This extra lens is placed further away from the sample to leave the sample space free of the magnetic field, and it is usually referred to as the Lorentz lens. The tradeoff is the loss of resolution (due to much higher aberrations), going down to about 1 nm for imaging and it is (in some of the techniques) even further reduced for acquiring the magnetic contrast.

During the TEM imaging, a thin sample is illuminated with a parallel electron beam. If the sample is magnetic, then its interaction with the electron beam can be understood in terms of the Lorentz force, of which the magnetic part is:

$$\boldsymbol{F} = -e(\boldsymbol{v} \times \mathbf{B}). \tag{2.1}$$

Considering a specimen of thickness t with in-plane magnetic domains, and with the saturation induction of the magnetic material B, the magnitude of the Lorentz deflection angle β is given by

$$\beta = \frac{eB\lambda t}{h}, \tag{2.2}$$

where e is the positive elementary charge, h is the Planck's constant, and λ is the electron wavelength [25–27]. The consequences of the electron deflection in the magnetic field of the sample can be used for the two basic imaging modes in Lorentz microscopy: the Fresnel mode and Foucault mode. Further use can be implemented in the scanning mode of TEM for acquiring the so-called differential phase contrast. These three methods will be described in the following subsections.

Fresnel mode

When a magnetic sample is imaged with the microscope's optics correctly focused, there is no observable magnetic contrast. The Fresnel mode is the easiest method of achieving magnetic contrast because it only uses defocusing of the Lorentz lens. Under these conditions, the magnetic domain walls are imaged as alternate bright (convergent) and dark (divergent) lines. The bright lines occur when the domain walls are positioned such that the magnetization on either side deflects the electrons towards the domain wall. The vectorial product nature of the Lorentz force yields no contrast related to the out-of-plane magnetization component. This is unfortunate for imaging the magnetic vortex cores. Images of the magnetic vortex show a white/black spot at the vortex core position, but the contrast gives the circulation, not polarity. Determination of the vortex polarity was also presented, but it was based only on the small displacement of the intensity spot to the opposite directions for opposite polarities when the sample was tilted [28]. The Fresnel mode is useful for real-time studies of magnetization reversal, as it is relatively easy to implement and can provide a frame rate up to approx. 1 Hz, depending on the camera settings. However, this mode does not provide any direct information about the magnetization direction within the sample. In case we want to match the Fresnel images to magnetization maps, we must calculate the magnetic contrast. This can be done with the Micromagnetic Analysis to Lorentz TEM Simulation (MALTS [29]), which is an open-source toolbox using magnetization vector files, typically calculated by micromagnetic simulators (e.g., OOMMF), as inputs.

It should be noted that the spatial resolution is not high (typically around 50 nm) because the images must be recorded at a relatively high value of objective lens defocus (in the mm range) to provide sufficient contrast [30]. Changing the defocus sign (i.e., going between underfocusing and overfocusing) reverses the contrast. underfocus. Example images acquired from NiFe rectangles and disks using the Fresnel mode are presented in Fig. 2.1.

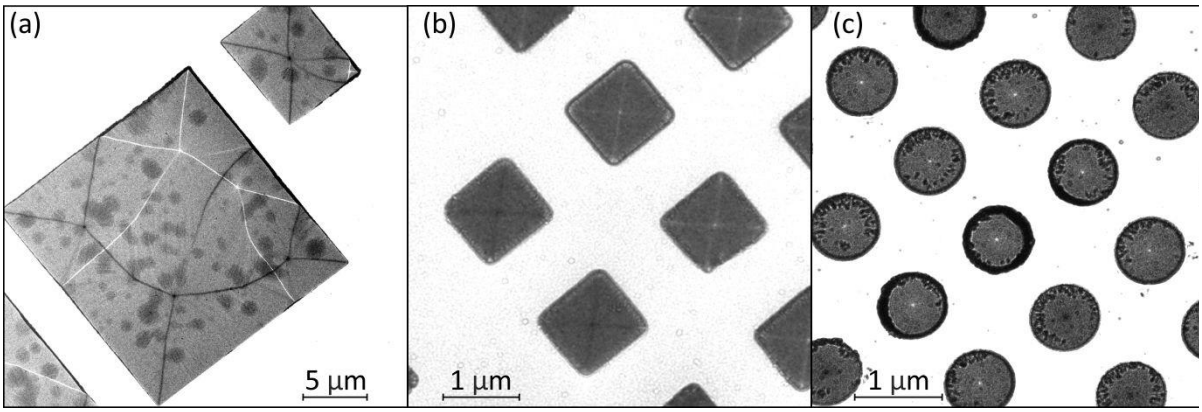

Fig. 2.1: Examples of Fresnel LTEM imaging performed on FEI Titan: (a) domain structure in larger patterns, (b) Landau patterns in 1 µm squares, (c) vortex states in 500 nm disks. The contrast does not provide any direct information about the local direction of magnetization but rather highlights the domain walls' positions. In the case of the disks, white/black dots at the center provide the position of the vortex core (but not its polarity), and the color depends on the circulation being opposite for white and black.

2.2 Magnetic Transmission X-ray Microscopy (MTXM)

Magnetic Transmission X-ray Microscopy (MTXM) is one of the types of X-ray microscopy techniques used for magnetic imaging of nanostructures. The contrast is provided by the X-ray Magnetic Circular Dichroism (XMCD), which is the X-ray absorption cross section's dependence on the relative orientation between the helicity of the photon beam and the projection of the magnetization in a ferromagnetic specimen onto the photon propagation direction [31,32]. Its physical origin is closely related to the polar magneto-optical Kerr effect. However, because for the XMCD, the initial state is a well-defined core level state, XMCD features an element-sensitivity, and according to dipole selection rules, also a symmetry-selectivity [33].

The sources of the circularly polarized X-ray radiation, which is essential to observe XMCD contrast, are usually synchrotron storage rings, either at helical undulators or at bending magnets [31]. Our measurements were done at beamline 6.1.2 (XM-1) of the Advanced Light Source (ALS) in Berkeley, California. The X-rays emitted from a bending magnet enter the microscope that has an optical design similar to a conventional microscope using visible light – there is a source, a condenser, an objective lens, and a detector. However, because soft X-rays' refractive index is close to one, conventional lenses or mirrors cannot be used. Instead, Fresnel zone plates (circular gratings with a radially increasing line density, see [34] for details) are used to focus the X-ray radiation [31]. Our imaging was carried out with a spatial resolution of 25 nm at Fe L3 absorption edge (707 eV). In contrast to the full field microscope at the ALS beamline 6.1.2, there are also scanning transmission X-ray microscopes used at other beamlines or at other synchrotrons (e.g., BESSY at Helmholtz Zentrum Berlin).

Even though this method was used only for static imaging in this work, the pulsed nature of the synchrotron radiation also provides a good temporal resolution in stroboscopic experiments. The resolution is given by the length of the electron bunches circulating in the storage ring. For ALS, it is about 70 ps.

2.3 Electrical detection by anisotropic magnetoresistance (AMR)

The electrical detection techniques are here to accompany the magnetic imaging. It is a less demanding group of methods in terms of the necessary equipment, although the sample

fabrication process is often more difficult. When the electrical properties are dependent on the sample's magnetization state, we talk about magnetoresistance, i.e., a change of electrical resistance with changing the spin configuration inside magnetic structures. There are several types of magnetoresistance effects, of which the simplest one is the anisotropic magnetoresistance (AMR). It was discovered already in the 19th century by William Thomson (honored as Lord Kelvin) [35], but it is a useful detection technique even nowadays. It has rather small amplitude (about 1%) when compared to the other two most common types of magnetoresistance – giant [36] and tunneling [37] – which both exhibit changes in the order of tens to hundreds of percent. On the other hand, the giant or tunneling magnetoresistances are measured in heterostructures while AMR is always present as its resistivity only depends on the angle φ between the vectors of current density $\boldsymbol{j}$ and magnetization $\boldsymbol{m}$. If we suppose resistance $\varrho_{\parallel}$ for $\varphi = 0°$ and $\varrho_{\perp}$ for $\varphi = 90°$, it can be shown, that the resistivity depends on φ as the following function [35,38]:

$$\varrho(\varphi) = \varrho_{\perp} + (\varrho_{\parallel} - \varrho_{\perp}) \cos^2 \varphi. \tag{2.3}$$

Magnetoresistance, being a change in resistance, is often expressed as a percentage of the value at saturation. We can calculate its value from the measured resistance as

$$\mathrm{MR} = \frac{R - R_{\mathrm{sat}}}{R_{\mathrm{sat}}} \cdot 100\%. \tag{2.4}$$

3 Magnetic vortex nucleation states under static conditions

Experimental measurements of the nucleation states were carried out for NiFe disks with diameters ranging from 500 nm to 4 μm and thicknesses ranging from 20 nm to 100 nm. The disks were fabricated by electron beam lithography, evaporation, and lift-off process on 30 nm and 200 nm thick SiN membranes suitable for the Lorentz Transmission Electron Microscopy (LTEM), and the Magnetic Transmission X-ray Microscopy (MTXM), respectively. For the Anisotropic Magnetoresistance (AMR) measurements, we used undoped Si (100) as a substrate, and the disk fabrication was followed by a second lithography step in which a pair of Au contacts was fabricated in order to establish electrical connections to the disk.

3.1 Classification of magnetic vortex nucleation states

The nucleation states are the transition spin configurations in magnetic disks through which the magnetization proceeds between the fully saturated state and the fully nucleated vortex state. Before we provide any results about the nucleation of magnetic vortices, we have to classify the nucleation possibilities. For this purpose, we performed micromagnetic simulations of disks with varying diameters and thicknesses. We used OOMMF with the following parameters: cell size of $(4 \times 4 \times 4)$ nm^3, saturation magnetization $M_s = 800$ kA/m, and exchange constant $A = 13$ pJ/m. Our simulation data show that three distinct nucleation pathways are possible, and Fig. 3.1 shows the three corresponding nucleation states. The first nucleation state, the **C-state** [39], is shown in Fig. 3.1(a). It consists of spins following the C letter's shape to decrease the dipolar energy compared to the disk in saturation. This state is common for small disks (approximately for diameters $D < 400$ nm and thicknesses $t < 20$ nm). The C-states are not so interesting to observe for their low complexity, and because of

their size, they are hard to probe because the disk sizes below 1 µm are usually on the limit of our imaging methods. In our work, we focus on two other nucleation states that can be found in larger disks: the **vortex-pair state** [40] and the **buckling state** [41–43] that are shown in Fig. 3.1(b), and Fig. 3.1 (c), respectively. So far, the evidence for these states was based on micro-Hall magnetometry [41] or AMR [42,43] measurements combined with micromagnetic simulations, but direct observation by magnetic microscopy methods was missing.

The vortex-pair state [Fig. 3.1(b)] is favored in intermediate disks with diameters $D > 400$ nm and thicknesses $t < 120{,}000\ \mathrm{nm}^2/D$ (the constant $120{,}000\ \mathrm{nm}^2$ was deduced from our analysis of LTEM images of arrays of different sized disks). However, the crossover between the vortex-pair state and the buckling state is continuous, and for each disk geometry in this work, we found both states with an increasing probability of finding the buckling state in large disks. The vortex-pair state consists of two vortex cores around which the magnetization is curling in the opposite sense (opposite circulations). Micromagnetic simulations show that the two cores of the vortex-pair state always have opposite polarities (giving the same handedness for both vortices of the pair). Upon the field decrease, the cores move towards each other, decreasing the net magnetization along the field direction until they annihilate, and a single vortex core is formed in the disk. As the polarity and circulation of the two competing vortices are opposite, the final vortex state will be random for symmetry reasons. However, this is difficult to realize in real samples because the geometrical symmetry can be broken due to lithographic imperfections and surface roughness of the substrate.

The buckling state [Fig. 3.1(c)] is favored in large disks. The buckling state's characteristic features are the three Bloch domain walls with in-plane magnetization curling around them. When the applied field is decreased, those three domain walls move towards each other until a vortex state is formed. The buckling state has a lower symmetry than the vortex-pair state, and the in-plane magnetization shape indicates the final circulation of the vortex – in the case of Fig. 3.1(c), the circulation will become counterclockwise. Even though the situation is less evident for the final polarity state, the simulations show that the m_z components at the disk edge will become dominant over those at the disk center – in the case of Fig. 3.1 (c), the vortex core polarity will be defined by the m_z component of the red domains.

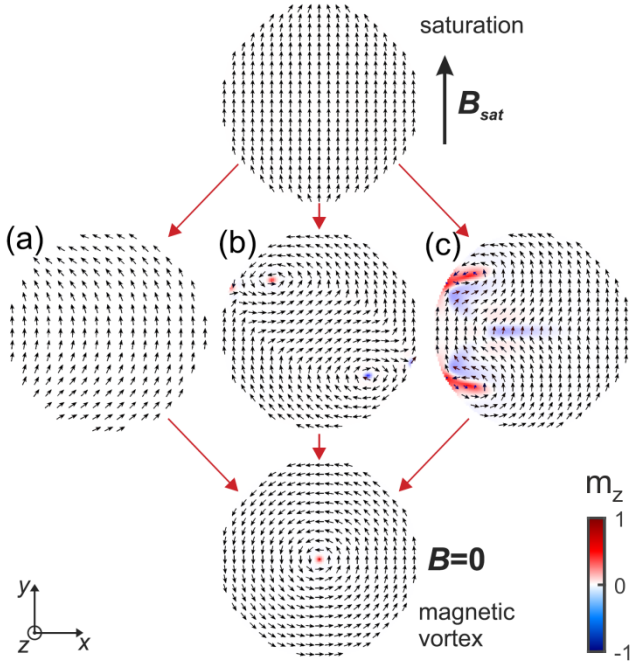

Fig. 3.1: Magnetic vortex nucleates upon the field decrease from saturation while undergoing one of the nucleation states visualized by micromagnetic simulations: (a) C-state, (b) vortex-pair state, and (c) buckling state. The blue-white-red color scale represents the perpendicular component of magnetization. Reprinted from [44].

3.2 Lorentz microscopy of the vortex nucleation states

The LTEM images (Fresnel imaging by defocusing) of the nucleation states were acquired using FEI Titan TEM at the accelerating voltage of 300 kV. The external magnetic field needed for vortex annihilation and subsequent gradual nucleation is applied by the TEM objective lens (which is normally turned off in the Lorentz mode). As this field is oriented along the microscope optical axis, the sample was tilted by 30 degrees to gain an in-plane magnetic field component. The tilt results in elliptical projections of the disks, and the necessary defocus causes further distortions that are observable in the images.

The ambiguity of indirect magnetization observation can be overcome by performing micromagnetic simulations of the corresponding magnetization states and comparing the calculated LTEM contrast to the measured data. We used Micromagnetic Analysis to Lorentz TEM Simulation (MALTS [29]) to compare the acquired images with micromagnetic simulations. Fig. 3.4 shows the important stages of the vortex nucleation modes in the top row, compared to the LTEM contrast images calculated by MALTS in the middle row. The source magnetization distributions simulated by OOMMF, from which the LTEM contrast was calculated, are shown in the bottom row of Fig. 3.4. LTEM images show a good agreement between the simulated and measured magnetic contrast for both the vortex-pair state stages [Fig. 3.4(a,b)] and the buckling state [Fig. 3.4(c,d)]. The C-state has no magnetic contrast in LTEM [Fig. 3.4(e)]. A reference vortex state at zero magnetic field is shown in Fig. 3.4(f).

The vortex-pair state nucleation process consists of two steps indicated in Fig. 3.4(a) and Fig. 3.4(b). The LTEM image in Fig. 3.4(a) is characterized by two lines, one with black and one with white contrast (in-plane domain walls) separating the three main domains containing the in-plane magnetization in the disk. Additionally, we can observe two intense spots at the disk boundary, where one of them is lighter and the other one darker than the background. They represent Bloch domain walls featuring a larger magnetization curl (i.e., higher contrast). Upon decreasing the field, the white and black lines move closer to each other until the Bloch domain walls unpin from the disk boundary into two standalone vortex cores yielding the spin configuration of the vortex-pair state in Fig. 3.4(b). Further field decrease leads to the formation of a single vortex. In case of the buckling state [Fig. 3.4(c,d)], the nucleation process is different. When the field decreases from saturation, the first step is forming Bloch domain walls at the disk boundary yielding bright LTEM contrast in these positions. From this state, the buckling state is formed by moving the two domain walls towards each other, which is accompanied by the gradual formation of a third domain wall at the disk center. The LTEM contrast then consists of a typical line passing through the disk center splitting towards the edge where the line bounces off the edge with reversed contrast [from black to white in case of Fig. 3.4(d)]. Further field decrease leads to the formation of a single vortex with polarity defined by the m_z component of the Bloch walls nucleated at the disk boundary.

The LTEM also shows two other aspects of the vortex nucleation. The first one is the pinning of magnetization present in a large portion of studied disks, leading to deformed nucleation states. However, after their study, we concluded that the number of nucleation modes is only seemingly higher than the three presented modes, but they all are only variations of the vortex-pair state or the buckling state which were caused by the pinning.

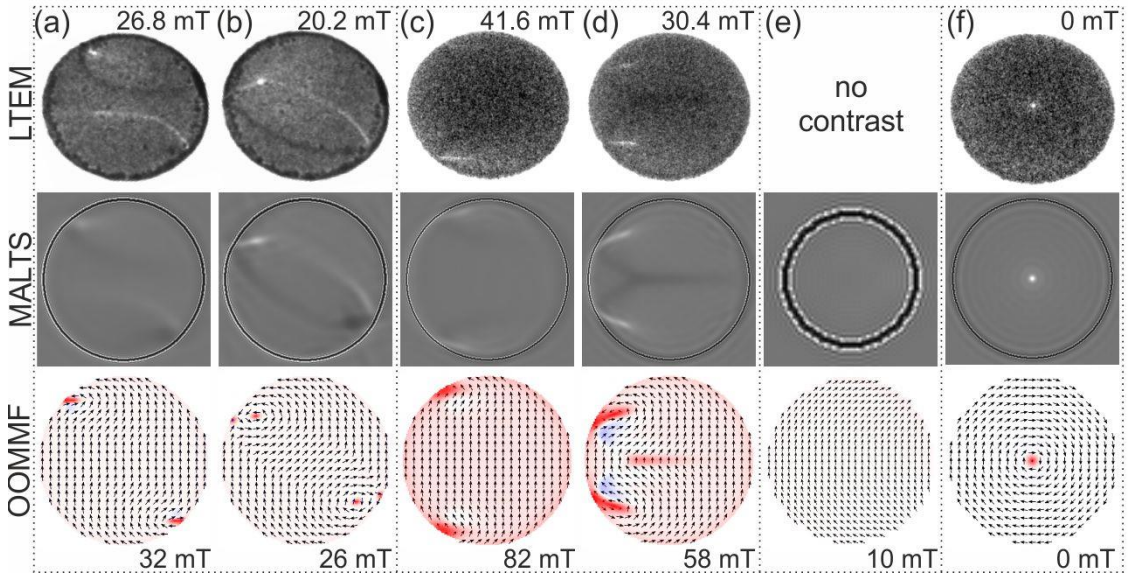

Fig. 3.2: Simulation and LTEM imaging of vortex nucleation states in magnetic field. The sample was tilted by 30°, and the indicated field values are the in-plane field components. Top row: LTEM observation; middle row: LTEM contrast simulated from the spin configurations shown in the bottom row: OOMMF micromagnetic simulations. The blue-white-red color scale represents the perpendicular component of magnetization. Columns: (a,b) Two consecutive configurations forming the vortex-pair state in a $D = 2$ µm, $t = 40$ nm disk. (c,d) formation of the buckling state in a $D = 2$ µm, $t = 100$ nm disk . (e) Simulations of the C-state in a $D = 200$ nm, $t = 16$ nm disk which does not show magnetic contrast in LTEM. (f) vortex state for reference. Reprinted from [44].

3.3 Electrical detection of vortex nucleation states

Alongside magnetic imaging, the nucleation processes were further studied by measuring the associated resistance changes due to AMR. This was performed by both numeric calculations and experimental measurements. We considered the symmetrical contact geometry presented in Fig. 3.3(a) with the magnetic field oriented along the *y*-axis. In this configuration, the highest resistance is measured at saturation, where the spins are aligned along both the applied field and the current density $\boldsymbol{j}$ (we neglide the current deviation from the y-asis for symmetrical contacts). Then each of the states comes with a lower level of electrical resistance following the AMR law for resistivity (AMR was also discussed in Section 2.3): $\rho(\varphi) = \rho_{\perp} + (\rho_{\parallel} - \rho_{\perp})\cos^2\varphi$, where φ is the angle between the vector of current density $\boldsymbol{j}$ and the vector of magnetization $\boldsymbol{m}$.

The OOMMF output files were used to calculate each state's resistance along the hysteresis loop to predict the shape and specific features of the measured data for the different nucleation processes going through the vortex-pair state or the buckling state. In the resistance calculation, we consider the direction of magnetization provided by the OOMMF magnetization map. The simulation gives the direction of magnetization at each point (cell) of the disk, but the problem arises from the current density direction. This can be calculated for constant resistivity materials (e.g., using COMSOL Multiphysics), but for non-constant resistivity caused by AMR, it presents a problem: the current density direction is dependable on the local resistivity and vice versa, which is much more difficult to solve. Our approach is considering that the resistance change is small, and thus we assume constant direction of current (homogenous current density in the whole volume for the simplest case of symmetrically placed contacts). Then we use each simulation cell's magnetization direction to calculate its resistivity and consecutively the resistance. Finally, we connect all of the cells as

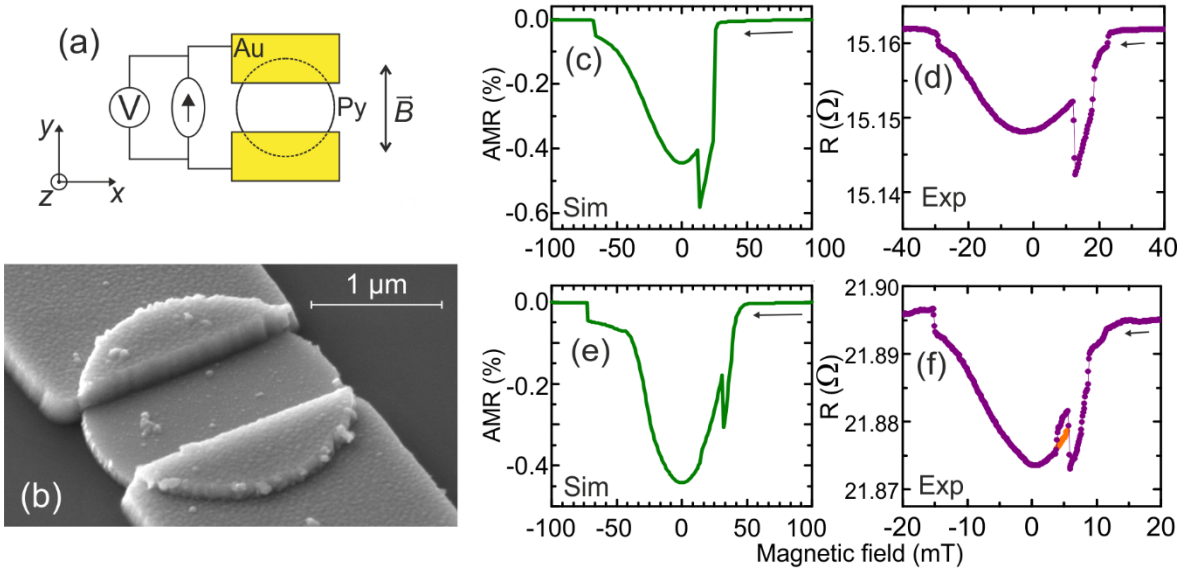

Fig. 3.3: Modeling and measurement of AMR data probing the magnetic vortex nucleation mechanisms. (a) schematics of the sample geometry with the electrical connection. (b) SEM image of a NiFe disk with gold contacts prepared by a two-step lithography process. (c-f) simulated and experimental AMR data of magnetic disks with nucleation via (c,d) the vortex-pair state ($D = 2$ μm, $t = 75$ nm disk) and (e,f) the buckling state ($D = 4$ μm, $t = 50$ nm disk).

a resistor network (cells connected in parallels and series) to obtain the total resistance value at each magnetic field.

Fig. 3.3(c,d) shows the simulated and experimental AMR data for vortex nucleation through the vortex-pair state. The magnetic field was swept in the direction from positive to negative field values. The simulated data in Fig. 3.3(c) show an abrupt resistance drop at 24 mT, where the vortex-pair state is formed in the disk, and then the resistance decreases linearly upon further lowering of the field. This is associated with the motion of the two cores of the vortex-pair state towards each other until the two cores annihilate into a single vortex state at 12 mT, leading to an abrupt increase of the resistance. The following curve represents the reversible displacement of the vortex core in a magnetic field. After reversing the field orientation, the annihilation occurs at -68 mT, where the resistance jumps up to the saturation level. The experimental data in Fig. 3.3(d) show the same features as those predicted by the simulation. The only difference is the nucleation part, where the resistance drops in several steps due to the pinning of magnetization (also observed during the LTEM imaging), which delays the formation of the vortex-pair state. The experimental values of the nucleation and annihilation fields are lower than the simulated values as the simulations are performed for 0 K.

The AMR data in Fig. 3.3(e,f) show similar general behavior compared to the data in Fig. 3.3(c,d), but several differences allow us to associate it with the buckling state nucleation process. One difference is in the first part of the nucleation process, where the resistance decreases gradually, without the abrupt drop all the way from saturation, where the buckling state is gradually formed. The other difference is in the larger depth of the resistance dip with respect to the resistance of the vortex state at zero field, in contrast to the shallower dip in the AMR data of the vortex-pair state. The nucleation occurs at 32 mT, where the resistance suddenly increases. A significant point of interest is at 15 mT, where a small drop in the

resistance is present. When inspecting the simulated states at each point around this drop, we found that the nucleated vortex state does not have a single vortex core but instead, there are two vortex cores with an antivortex in between them. This is called the vortex-antivortex-vortex (VAV) triplet, and its simulation is shown in Fig. 3.4. The VAV triplet is stable in a range of a few mT, and after further field decrease, it annihilates into a single vortex core resulting in a small drop in the AMR data. This state was electrically detected with a typical peak shown in the purple curve shown in Fig. 3.3(f) between 4-6 mT. However, when the measurement was repeated multiple times, this peak was present only in about 30% of all field sweeps, while the other field sweeps in this range followed the green trace in Fig. 3.3(f). This is attributed to the VAV triplet's lower stability compared to the vortex state with a single core at the same magnetic field.

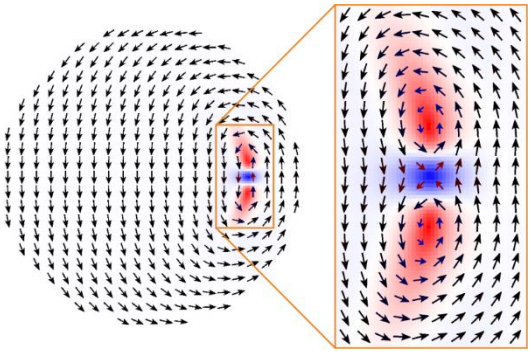

Fig. 3.4: Simulation of the vortex-antivortex-vortex (VAV) triplet with detail on the right side. The blue-white-red color scale represents the perpendicular component of magnetization.

4 Vector network analysis in magnetization dynamics experiments

In this chapter, we will introduce the measurement device crucial for the following experimental chapter: **the vector network analyzer (VNA)**. It generates and detects high-frequency signals with the maximum possible operating frequency exceeding 100 GHz. VNA consists of ports to which a sample, commonly called a device under test (DUT), is connected using high-frequency cables, or high-frequency probes.

In general, VNAs can have multiple ports, but there are typically only two ports necessary for carrying most of the experiments in the field of magnetism. Therefore, the following description will be limited to a 2-port VNA, but can be extended to a multi-port VNA if needed.

VNA, in contrast to an oscilloscope, works directly in the frequency domain. Instead of the signal's time dependence, it measures the signal amplitude and its phase shift with respect to the excitation signal. However, these two quantities (amplitude and phase) can carry the desired information from the sample with the advantage of a much higher reachable frequency than any oscilloscope can reach. VNA can also test the sample's response for a wide frequency range in a very short time, typically testing hundreds of frequency measurements per second, depending on the detectors' bandwidth settings.

4.1 The function of a vector network analyzer

Wave quantities and S-parameters

VNA generates a sinusoidal test signal a_j, often called stimulus, which is applied to the DUT. The signal at the DUT undergoes three basic processes: reflection, absorption, and transmission resulting in a signal b_i, which will be (at least in the case of a linear DUT) sinusoidal as well. Here, the subscripts i, j stand for port numbers 1 and 2. An example of the wave quantities is shown in Fig. 4.1. Both signals a_j and b_i are measured using receivers described later in this chapter. As we do not use active devices, the received signals b_i will always be smaller than test signals a_j, and generally may be phase shifted with respect to each other. In the measurement, the quantities are usually represented using the complex scattering parameters – S_{ij}-parameters. They provide transition from the generated signals represented by an a-vector to the detected b-vector using the following matrix multiplication:

$$\begin{pmatrix} b_1 \\ b_2 \end{pmatrix} = \begin{pmatrix} S_{11} & S_{12} \\ S_{21} & S_{22} \end{pmatrix} \begin{pmatrix} a_1 \\ a_2 \end{pmatrix} \tag{4.1}$$

Here, it is apparent that S-parameters with the same indices (S_{11} and S_{22}) connect wave quantities from the same port, and therefore they represent the reflection of microwaves from the DUT back to the same port. On the other hand, the remaining S_{21} and S_{12} parameters connect wave quantities from both ports and represent microwave transmission from one port to the other. The parameter S_{21} represents the transmission from Port 1 to Port 2 and is called the forward transmission, while S_{12} represents the opposite direction and is called the reverse transmission. During the measurement, there is always only one active output at the time, i.e., a_1 and a_2 are not active at the same time.

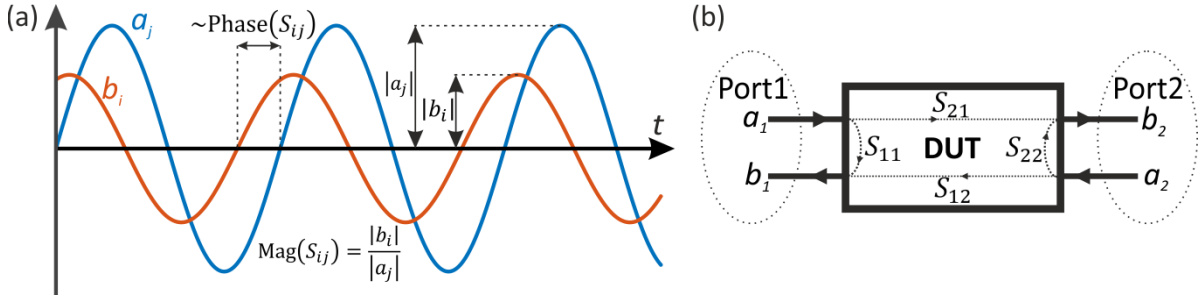

Fig. 4.1: (a) Illustration of the generated and detected wave quantities. (b) Schematics of S-parameters using wave quantities on a 2-port VNA. S_{21} represents the forward transmission from Port 1 to Port 2 and S_{12} represents the reverse transmission from Port 2 to Port 1.

The S-parameters are complex numbers; the absolute value of the complex number represents the magnitude, and the argument (angle of the vector representing the complex number in the Gauss plane) represents the phase:

$$|S_{ij}| = \frac{|b_i|}{|a_j|} \equiv \text{magnitude}, \tag{4.2}$$

$$\arg(S_{ij}) = 2\pi f \Delta t \equiv \text{phase}. \tag{4.3}$$

It is important to note that because the S-parameters are ratios of two signals, they are unitless. For the sake of readability, we will rewrite the representation of magnitude and phase as follows:

$$\text{Mag}(S_{ij}) = |S_{ij}|, \tag{4.4}$$

$$\text{Phase}(S_{ij}) = \arg(S_{ij}). \tag{4.5}$$

VNA receiver operation

A typical 2-port VNA instrument is represented with the schematics shown in Fig. 4.2. Firstly, one microwave generator is shared for both ports using microwave switches, and then there are two receivers per port: one measures the generated wave as a reference while the second one measures the scattered signals coming back to the port from a DUT. These two signals are selected in a directional element represented with the yellow boxes in the schematics (Fig. 4.2).

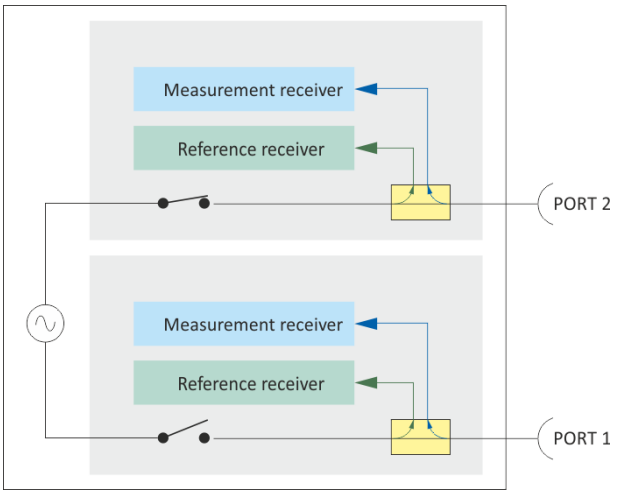

Fig. 4.2: Schematics of a 2-port VNA. The two ports share the same microwave generator. Each port then has its own reference and measurement receivers tracking the signals directed by the directional element (yellow box). Reprinted from [45].

4.2 Excitation structures (antennas) in magnetic experiments

The VNA based methods conventionally rely on driven (coherent) excitation of magnetization dynamics by a microwave magnetic field. Electromagnets are not useful tools for this job as they have high inductance limiting the maximum operating frequency. Therefore, we need to use a simpler device with minimal inductance that can be powered by the VNA's generator. The desired capability is the high-frequency operation and microwave field localization allowing us to excite also non-zero k-vectors (spin-waves). Together we will call these structures antennas even though it does not fulfill the standard definition being a transmission device used to broadcast signals between locations. The three basic types used in this work are striplines, coplanar waveguides, and ground-signal (GS) antennas, all of which are described in the following paragraphs.

When designing the excitation antennas, we should keep in mind the characteristic impedance of the VNA's ports ($50\ \Omega$) to which the geometry needs to be matched to suppress unwanted reflections. For this purpose, we use the freeware TX line software [46], providing calculation tools for standard microwave structures based on the geometry and substrate material's permittivity. In the case of more complicated designs, it would be necessary to perform a finite element analysis or simply take a qualified guess based on previous experience.

When exciting spin waves, the source of excitation must match both the temporal and spatial frequency of the spin-wave mode. The spatial profile of the magnetic field created by the antenna dictates the ensemble of k-vectors, that the structure can excite. Thus, for all of the antenna types, we will be interested in their excitation spectra, represented by the excitation efficiency J_{exc}, which provides the degree of excitation for every k-vector. The

spectrum can be calculated as a Fourier transform of the magnetic field's spatial distribution produced by the antenna's conductive lines. Therefore, it is essential to know the magnetic field distribution first, which typically requires finite element analysis. However, very good estimations were presented in the appendix of [47]. Despite the crude simplification relying only on the distribution of the current density $\boldsymbol{j}$, it provides very accurate results. The spectra shown below were calculated from the current density distributions (for striplines, CPWs, and GS antennas).

Comparison of the excitation spectra

Here we will compare the excitation spectra of the mentioned antenna types. The excitation spectrum of each of them is plotted in Fig. 4.3. One of the differences is that striplines can excite FMR ($k = 0$) whereas CPW and GS cannot. The graph shows that CPW's and GS's excitation spectra are very similar. The GS antenna has slightly broader peaks. Striplines are more often chosen when there is a need for a continuum of excited k-vectors. On the other hand, if we require very high k-vector numbers, we have to shrink the stripline width, which brings higher lithography requirements, and it is also less effective because of its resistance increase. The excitation of high k-vectors is easier with CPW or GS antenna, where the spectrum depends on all geometrical parameters, but it is more difficult to fabricate for minimal dimensions, especially with small gaps in the order of 100 nm or less.

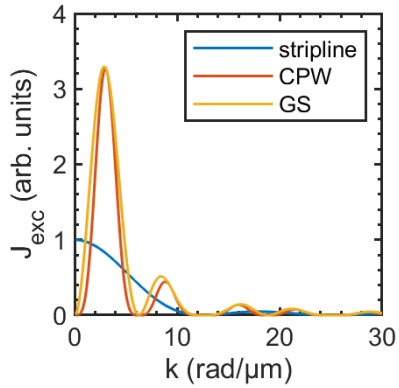

Fig. 4.3: Comparison of the excitation spectra J_{exc} for stripline antenna, coplanar waveguide and GS antenna. All calculation dimensions are 500 nm ($l_s = l_{gap} = l_{GND} = 500$ nm).

4.3 Ferromagnetic resonance measured on VNA

Ferromagnetic resonance (FMR), being the collective oscillations of magnetic spins, is the simplest case of high-frequency excitation. Historically, the first FMR experiments used a microwave resonant cavity placed in the gap of an electromagnet [48]. The incident microwaves drive the cavity to resonance, and the microwave photons then excite the magnetic sample. The observed quantity is the reflected microwave power at a given magnetic field. Although such resonant systems are very sensitive, the main disadvantage lies in the cavity's very narrow frequency band of operation. The only variable parameters in the experiment are the external magnetic field and the respective angle of the sample to the external magnetic field direction.

Modern FMR experiments often use a VNA and planar excitation structures like the before mentioned striplines and CPWs. Here both the frequency and magnetic field can be swept in an extensive range providing much more data for detailed analysis. The method is usually called the broadband VNA-FMR. The main principle remains the same: a microwave source excites the sample, this time using the high-frequency field of a stripline or CPW, and then the microwave transmission through the CPW is detected on the second VNA port. There

is also no need for complicated sample installation as it is simply placed over the waveguide with the studied layer facing down (so-called flip-chip method).

There is a variety of fixtures providing an interface for the VNA-FMR experiment. In our lab, we use a CPW fabricated onto a GaAs substrate utilizing electron beam lithography and electron beam evaporation. The parameters of the CPW were calculated using the TX line (freeware) software to match the impedance of the VNA. The CPW is interfaced to the VNA using microwave probes, which is schematically shown in Fig. 4.4.

An alternative is to the flip-chip method is to fabricate a permanent fixture with a waveguide contacted to RF connectors. Therefore, there would be no need for microwave probes. This approach can be superior because such a fixture with metalized vias and a well-defined ground plane can exhibit an almost flat frequency response. Nevertheless, it is far more challenging to design and fabricate it because employing more advanced RF system knowledge is required. On the other hand, the microwave probes are supplied with a complete calibration method, and even if the fabrication of self-developed CPW fixtures was not possible, every calibration substrate is equipped with a long CPW transmission line of very high quality that can be used precisely for this purpose with no need for in-house lithography.

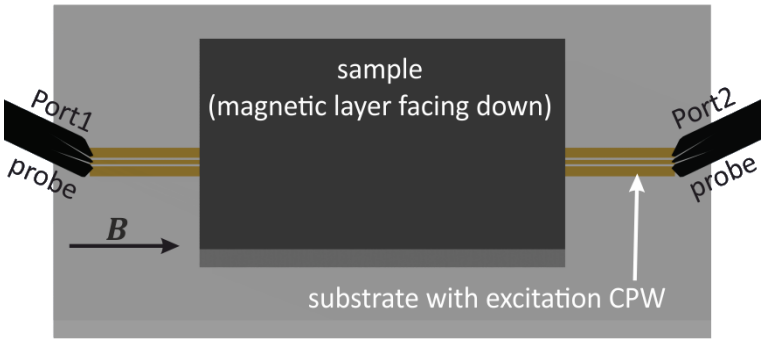

Fig. 4.4: Schematics of the VNA-FMR experiment. The coplanar waveguide is connected to the VNA using a pair of microprobes. The external magnetic field is aligned with the CPW, onto which the sample is placed with the magnetic layer facing down.

Data processing

The ferromagnetic resonance is observed as a dip in the frequency spectrum of the transmission signal magnitude $\mathrm{Mag}(S_{21})$. This dip represents an energy loss because the power is used to excite the ferromagnetic resonance. There are also other sources of frequency-dependent energy dissipation; thus, the measured FMR signal is modulated onto a non-even background. It is profitable to use a suitable data processing method to suppress the non-magnetic background, which is constant over the magnetic field. The simplest method by far is to divide the measured transmission magnitude by a reference. The most straightforward reference acquisition can be made by increasing the magnetic field high enough that the FMR peak goes out of the measured frequency range. This is often hardly possible in our case of the 380 mT maximum field and a 50 GHz VNA. A useful alternative is to calculate the reference as the median value of the measured signal magnitude for all magnetic fields at every single frequency because the median well reflects the background value:

$$\div \mathrm{Mag}(S_{ij}) = \frac{\mathrm{Mag}(S_{ij})}{S_{ij}^{\mathrm{ref}}}, \quad S_{ij}^{\mathrm{ref}} = \mathrm{median}_B\left[\mathrm{Mag}(S_{ij})\right]. \tag{4.6}$$

We will use the division symbol ÷ to annotate this kind of processing (opposite to signal subtraction, annotated Δ, which is used in the data processing of PSWS, Section 4.4). After

applying this procedure, the signal value is relative to the background, which now has a value of 1.

Extraction of saturation magnetization M_s and gyromagnetic ratio γ

The main goal of FMR measurement is usually extraction of the basic material parameters: Saturation magnetization M_s and gyromagnetic ratio γ. This can be done by fitting the peak positions f_{FMR} by the Kittel formula (also previously presented in Section 1.4):

$$f_{\mathrm{FMR}} = \frac{\gamma}{2\pi}\sqrt{(B_{\mathrm{ext}} + B_0)(B_{\mathrm{ext}} + B_0 + \mu_0 M_S)}. \tag{4.7}$$

The field offset B_0 is typically non-zero even for non-anisotropic materials like NiFe or CoFeB because there usually is a small residual magnetocrystalline anisotropy. Another contributing factor to B_0 is the shape anisotropy. Therefore it should not be omitted in the fit. Fig. 4.5 shows the processed VNA-FMR data and their fits using Eq. (4.7) for our three most used materials: NiFe, CoFeB, and YIG, all fitted for M_s, γ, and B_0. The fits reproduce the data with remarkable agreement, and the resulting fit coefficients are reasonable and non-deviating from the known values. However, we should be cautious when using unconstrained fits because the constants M_s, and γ are highly dependent on each other, and the fit may yield inaccurate results for some samples even when the fit exhibits a very low deviation from the experimental data. This problem can be solved by fixing either M_s or γ at a known level and fitting only the remaining one together with the field offset B_0.

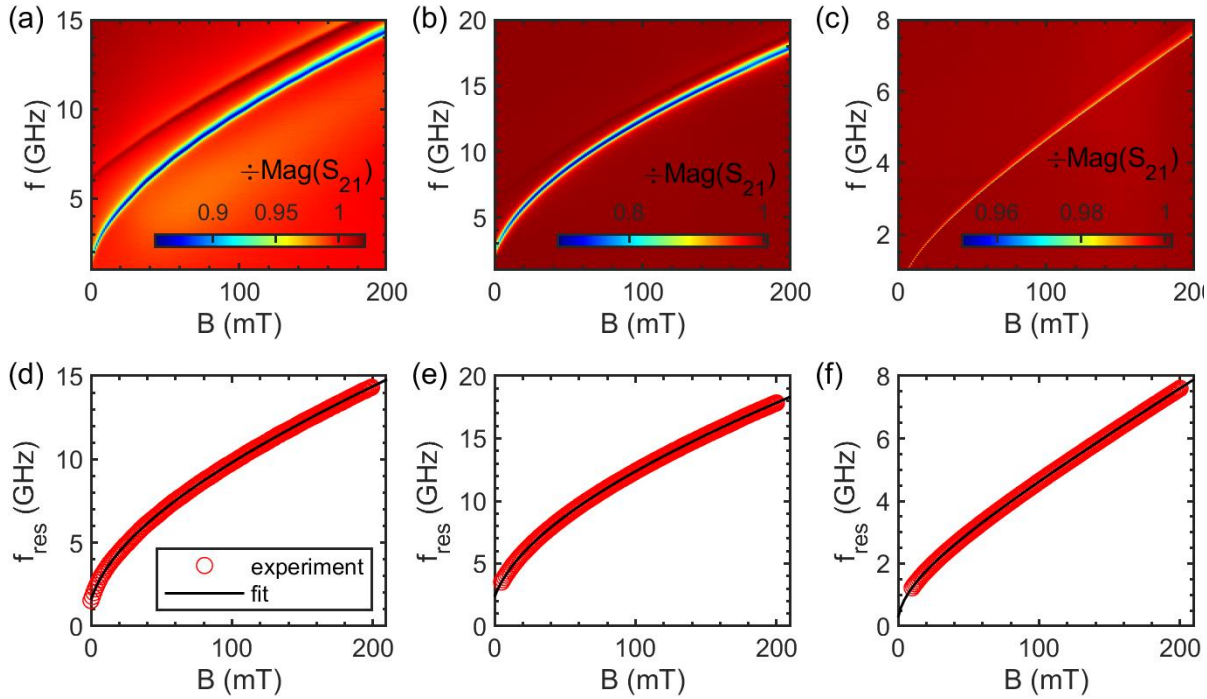

Fig. 4.5: VNA-FMR scans fitted with the Kittel formula Eq. (4.7) for (a) NiFe 100 nm, (b) CoFeB 100 nm, (c) YIG 100 nm. (a,b) have visible PSSW bands above the FMR band. Measurements were performed in a decreasing magnetic field.

Fit parameters:

(d) NiFe 100 nm: $M_s = 801$ kA/m ($\mu_0 M_s = 1.01$ T), $\gamma/2\pi = 29.0$ GHz/T, $B_0 = 2.85$ mT

(e) CoFeB 100 nm: $M_s = 1.20$ MA/m ($\mu_0 M_s = 1.51$ T), $\gamma/2\pi = 30.2$ GHz/T, $B_0 = 4.00$ mT

(f) YIG 100 nm: $M_s = 142$ kA/m ($\mu_0 M_s = 0.178$ T), $\gamma/2\pi = 27.6$ GHz/T, $B_0 = 0.55$ mT

4.4 Propagating spin-wave spectroscopy (PSWS)

The propagating spin-wave spectroscopy (PSWS) is a VNA-based technique utilizing a pair of microwave antennas (stripline, GS, CPW) to study spin-wave propagation. One of the antennas is powered by the VNA's microwave source and excites spin-waves, propagating over the gap. The second antenna serves as an induction pick-up detected by the VNA's second port.

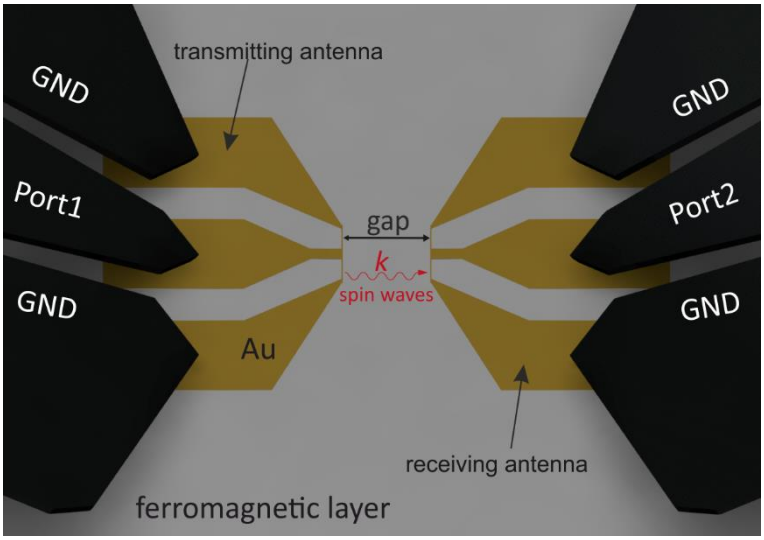

Fig. 4.6: Schematics of the PSWS experiment. A pair of microwave antennas is connected to a VNA using microwave probes. One antenna excites spin-waves in the magnetic layer underneath in which the waves propagate over the gap distance and are detected using the induction pick-up of the second antenna.

Data Processing

The raw S-parameters, as they are measured by the VNA, carry the PSWS signal that is modulated onto a non-magnetic background. The background is always present in the experiment due to the crosstalk between the antennas. It should be constant over the magnetic field and therefore can be subtracted by a reference signal S_{ij}^{ref}. The reference can be either measured as a high magnetic field sweep (signals are out of the frequency range) or calculated as the median value of the real and imaginary S_{ij} components over all measured magnetic fields (the median value well reflects the background level), providing the processed signal ΔS_{ij}:

$$\Delta S_{ij} = S_{ij} - S_{ij}^{\mathrm{ref}}, \quad S_{ij}^{\mathrm{ref}} = \mathrm{median}_B\left[\mathrm{Re}(S_{ij})\right] + i \cdot \mathrm{median}_B\left[\mathrm{Im}(S_{ij})\right]. \qquad (4.8)$$

Example results of the S_{21} signal measured on a 30 nm thick CoFeB layer over the gap distance 1.8 µm using the $\boldsymbol{k} \perp \boldsymbol{M}$ geometry and 500 nm wide striplines is shown in Fig. 4.7(a,b,c). Processed ΔS_{21} data is then shown in Fig. 4.7(d,e,f). The signal is stronger in the $+B$ part of the spectrum because this geometry is known to be non-reciprocal, which will be discussed later.

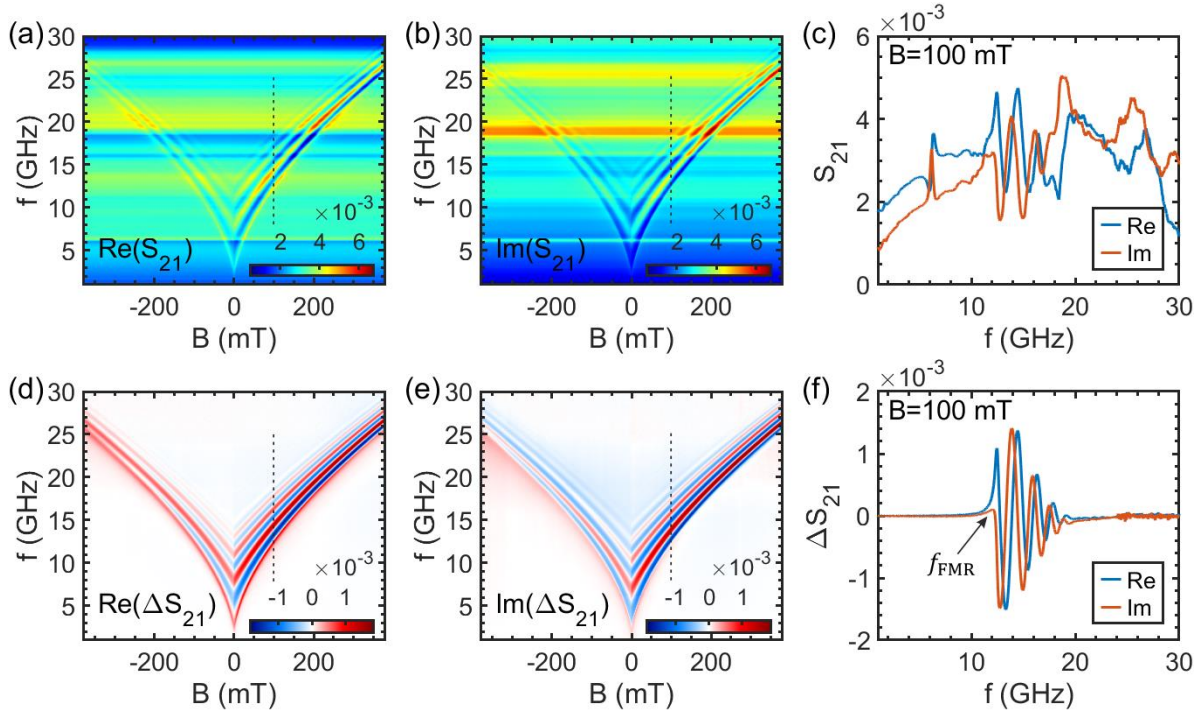

Fig. 4.7: PSWS data processing. The measurement was performed at $\boldsymbol{k} \perp \boldsymbol{M}$ geometry showing the spin-wave non-reciprocity – the signal is stronger for the positive magnetic field than the negative magnetic fields. (a,b) real and imaginary parts of raw S_{21}, (c) an example S_{21} sweep at magnetic field $B = 100$ mT. The magnetic signal is modulated onto a background signal, which is constant over all magnetic fields. (d,e) real and imaginary parts of processed (subtracted) ΔS_{21}, (f) ΔS_{21} sweep at magnetic field $B = 100$ mT. Background of the processed signal is zero, and the spin-wave signal is expressed in the form of oscillations in the real and imaginary parts of ΔS_{21}, showing the changing phase.

5 Spin-wave dispersion relations measured by VNA

The previous chapter presented the PSWS experiment (Section 4.4), which will be the basis for evaluating the spin-wave dispersion relations presented in the following sections. All of the fitted dispersions use the dipole-exchange model presented in Section 1.7 with totally unpinned surface spins (except for the hybridized modes).

5.1 Spin-wave dispersion extraction using the PSWS experiment

This work is not the first attempt to evaluate the dispersion from a PSWS measurement. In previous reports, the spin-wave dispersion was extracted from YIG by using the CPW excitation. As the CPWs excitation spectrum exhibits distinct peaks, it allows extracting one point in spin-wave dispersion for each of the CPWs excitation spectrum peaks. The central k-vector of each excitation spectrum peak is then assigned to a frequency from either the envelope of the S_{21} sweep [49,50] or by fitting the S_{21} spectrum [51]. This approach is limited to only several extracted points, and is not easily transferable to metallic materials because of the low signal amplitude when compared to YIG due to large damping in metallic layers,

making it impossible to use more than two peaks from the excitation spectrum. There was also an attempt to evaluate the dispersion from a single VNA sweep [52,53] by applying the equation:

$$k(f) = \frac{\Delta\varphi_{\mathrm{SW}}(f)}{L}, \tag{5.1}$$

where φ_{SW} is the spin-wave phase and L is the distance over which the phase is measured. This approach requires to know the precise distance over which the spin-wave changes its phase, which is challenging to evaluate because the measured phase difference can be offsetted by a measurement-related and frequency-dependent phase offset. We can write the phase difference as

$$\mathrm{Phase}(\Delta S_{21}) = \varphi_{\mathrm{SW}} + \varphi_0, \tag{5.2}$$

where ΔS_{21} is the VNA transmission signal with subtracted background using Eq. (4.8). The offset φ_0 is not needed in the routine described below, where only a relative phase change is necessary to know. Another limitation hides in the maximum measurable k-vector, which will be $k_{\max} = \pi/L$ because the phase is measured in the $-\pi$ to $+\pi$ interval and the real phase change over the distance L will not be possible to determine correctly from the measurement for larger $k > k_{\max}$ (at least for excitation antennas with non-continuous excitation spectrum, e.g., CPWs or even ladder antennas, where the phase cannot be unwrapped in the frequency spectrum, see the discussion below).

Our approach uses multiple measurements of the spin-wave phase over several gap sizes g between the antennas. Subsequently, we assume a single plane wave propagating in the layer, and that the measured phase difference at each frequency evolves linearly with the relative change of the gap size, which is reflected in Eq. 5.1. Because the relative change of the gap size g is a controlled parameter (in the design used for lithography) and the phase difference $\mathrm{Phase}(\Delta S_{21})$ is extracted from the VNA measurement, we can fit the following equation, where the slope of the fit is identified as the spin-wave k-vector:

$$\mathrm{Phase}(\Delta S_{21}[g, f]) = k(f)g + \varphi_0(f), \tag{5.3}$$

The phase offset φ_0 is the fit intercept. Therefore, for executing this method, we need to fabricate multiple antenna pairs with varying gap g. The magnetic entity for which we want to evaluate the spin-wave dispersion needs to be as identical as possible for each pair of antennas. This is easily achievable for the continuous magnetic layers at which we focus, yet it can be problematic when applying this approach to magnetic nanostructures. The phase is calculated from the subtracted transmission data; an example of phases measured over multiple gap distances on CoFeB 30 nm thin film is shown in Fig. 5.1(a). Correct data subtraction is critical because it affects the quality of the calculated phase of the spin-wave, and both the random and systematic errors can create artifacts in the dispersions. Therefore, the data must be acquired carefully, minimizing undesirable effects of, e.g., probe contacting or temperature (mentioned in Section 4.4).

The example phase measurements $\mathrm{Phase}(\Delta S_{21})$, plotted in Fig. 5.1(a), start changing after the frequency reaches the FMR frequency at approx. 12 GHz, and the slope of the curve is higher for larger gaps. I.e., the lowest measured phase corresponds to the smallest gap and the uppermost to the largest measured gap size. Then we plot all the measured phases for each frequency against the gap sizes g between the antennas [representative frequencies are plotted in Fig. 5.1(b)]. It shows linear phase dependencies that can be easily fitted, as was explained, with the slopes of the lines equal to the k-vector. Now we can finally plot the extracted k-vectors against their respective frequencies, showing the resulting dispersion relation in Fig. 5.1(c).

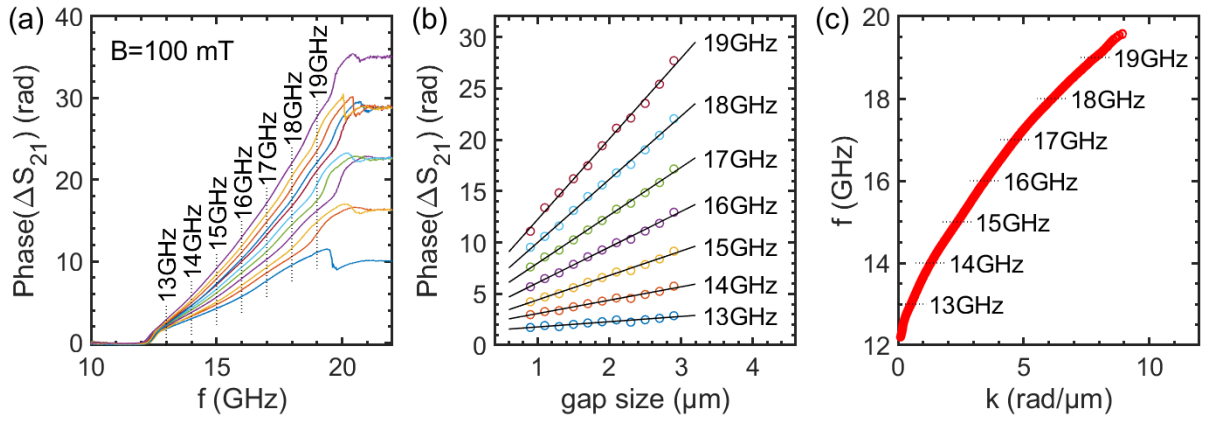

Fig. 5.1: Extraction of the dispersion from the PSWS experiment on CoFeB 30 nm layer. (a) unwrapped ΔS_{21} phases measured over several gap distances from 0.9 μm (the lowest line) to 2.9 μm (the steepest line) with the step of 200 nm. (b) representative fits of the phase where the fit's slope yields the desired k-vector at that frequency. (c) dispersion relation extracted for all frequencies within the range with sufficient PSWS signal.

5.2 Spin-wave dispersion of NiFe layer

The first material on which we tested the spin-wave dispersion measurement was a NiFe layer. The material is known for its relatively short spin-wave propagation lengths (due to relatively small magnetization and high damping), but measuring it in the PSWS experiment was non-problematic. Fig. 5.2(a,b) shows representative data in the $\boldsymbol{k} \perp \boldsymbol{M}$ geometry. The background has a slight magnetic field dependence, which is visible in the lightly red-colored ($\sim 10^{-5}$ signal level) top right corner in Fig. 5.2(a,b). It was identified as an experimental setup-related issue. Fig. 5.2(c) shows the experimentally evaluated dispersion relations for the magnetic field from 20 mT to 200 mT. The evaluated dispersions were fitted using the dipole-exchange model with reasonable agreement. The maximum detected k-vector was slightly below 10 rad/μm but the 200 nm wide stripline should theoretically excite k-vectors up to approx. 20 rad/μm. We attribute this to the high attenuation in NiFe and the decreasing propagation length with k-vector in the $\boldsymbol{k} \perp \boldsymbol{M}$ geometry.

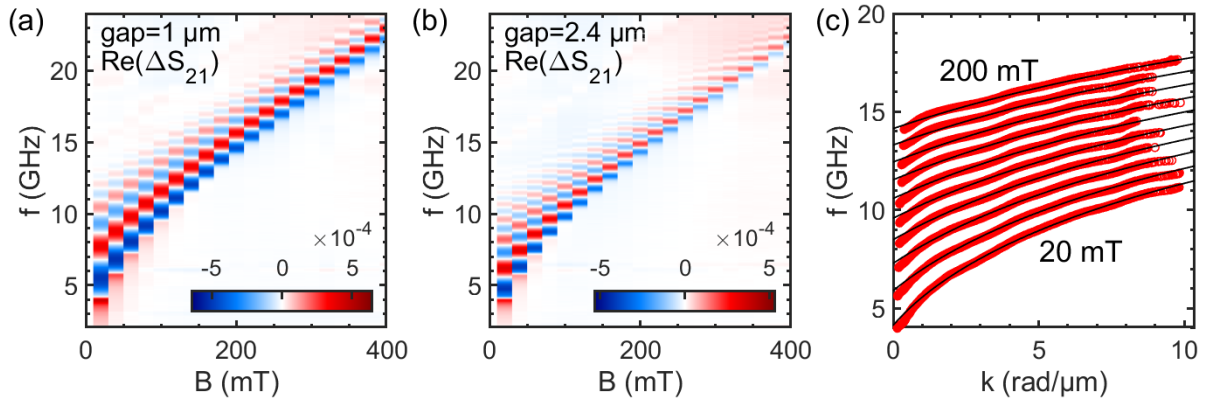

*Fig. 5.2: PSWS experimental data in $\boldsymbol{k} \perp \boldsymbol{M}$ geometry. **Material: NiFe 40 nm layer**, used antenna type: $l_s = 200$ nm striplines, used power: 5 dBm. (a,b) representative data. (c) extracted dispersion relations for fields from 20 to 200 mT with 20 mT step with fit using the dipole-exchange model. Measured gaps: 1.00, 1.11 1.24, 1.38, 1.55, 1.73, 1.93, 2.15, 2.40, and 2.68 μm.*
Fit parameters: $\gamma/2\pi = 28.8$ GHz/T, $t = 34.1$ nm; fixed parameters: $M_s = 800$ kA/m ($\mu_0 M_s = 1.0$T), $A_{ex} = 16$ pJ/m.

5.3 Spin-wave dispersion of CoFeB layers

The thin 30 nm layers of CoFeB exhibit similar qualitative behavior to the previously measured NiFe. CoFeB has higher M_s and γ values, therefore the overall frequency range is above the one of NiFe, and importantly, the maximum measured signal is approx. 3x higher at comparable gap size (approx. $4 \cdot 10^{-3}$ for 30 nm CoFeB vs. approx. $5 \cdot 10^{-4}$ for 40 nm NiFe). Fig. 5.3(a,b) show representative experimental data in the $\boldsymbol{k} \perp \boldsymbol{M}$ geometry, and Fig. 5.3(c) shows the extracted dispersion relations fitted with the dipole-exchange model displaying good agreement. The maximum extracted k-vector is comparable to the NiFe measurement in Fig. 5.2(c) while the used stripline is wider ($l_s = 500$), which is because the signal is higher by one order of magnitude and therefore, lower excitation efficiency is required.

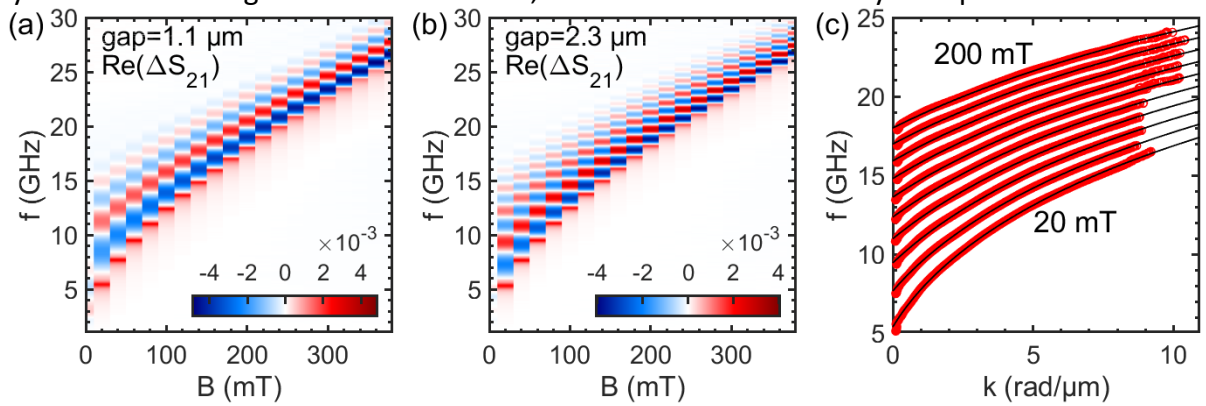

*Fig. 5.3: PSWS experimental data in $\boldsymbol{k} \perp \boldsymbol{M}$ geometry. **Material: CoFeB 30 nm layer**, used antenna type: $l_s = 500$ nm striplines, used power: 0 dBm. (a,b) representative data. (c) extracted dispersion relations for fields from 20 to 200 mT with 20 mT step with fit using the dipole-exchange model. Measured gaps: 0.9 to 2.9 μm with 0.2 μm step.*
Fit parameters: $M_s = 1.20$ MA/m ($\mu_0 M_s = 1.51$ T, $t = 29.6$ nm; fixed parameters: $\gamma/2\pi = 30.8$ GHz/T, $A_{ex} = 15$ pJ/m.

5.4 Summary of the spin-wave dispersion measurements

This chapter presented data on spin-wave dispersions that were measured by a VNA using the PSWS experiment. It proved to be a very powerful technique for characterizing magnetic layers' dynamic properties, which was demonstrated on NiFe, CoFeB, and YIG thin layers. Alongside the dispersions, data on propagation lengths were also presented.

Probing of advanced features, like the mode hybridizations in 100 nm CoFeB layers or the bandgap in FIB-modified NiFe layer creating a magnonic crystal, was also demonstrated. The hybridized dispersion modes proved to be a useful tool for evaluating the layers for the surface pinning parameter because the opening of hybridized modes is strongly dependent on the pinning. The pinning parameter is also not easy to obtain by other conventional methods.

6 Freestanding and positionable microwave antenna device

Previous chapters dealt with spin-wave excitation and detection, where the antennas (one antenna in case of BLS detection) had to be patterned on the sample. The fabrication of antennas directly on the sample can be a complex and time-consuming process requiring the availability of a nanofabrication facility. Moreover, some samples present extra challenges in the process of antenna fabrication, e.g., samples using single-crystal copper substrates used in [55,56], where the antenna parts can be easily short-circuited through the substate disabling it from spin-wave excitation. Another disadvantage of the classical approach is that the antenna is no longer repositionable after fabrication. This led to the idea of separating the excitation antenna from the sample itself by designing and fabricating an antenna device that would be freestanding with the ability to land to any position on the sample. Simultaneously, this device would have to allow optical detection by BLS or other techniques and navigation on the sample. Therefore the first design choice was to fabricate it on a transparent substrate. The main concept idea of this approach is shown in Fig. 6.1. The following paragraphs will describe its full design and use in optically and electrically detected experiments.

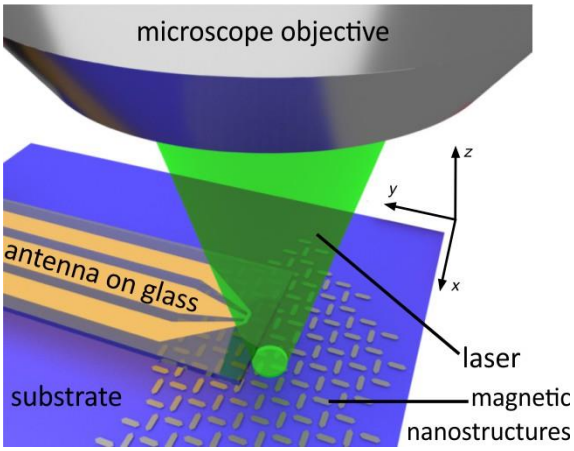

Fig. 6.1: Positionable antenna device with excitation part fabricated on a glass cantilever landed on a sample with magnetic nanostructures. Reprinted from [54].

6.1 Design and fabrication of the antenna device

Fig. 6.2(a,b) shows a side and top views of an antenna device model, where the device was designed to consist of three main parts:

1. thin glass cantilever with the excitation part,
2. printed circuit board (PCB) coupler,
3. SMA connector (Rosenberger 32K243-40ML5).

The glass cantilever is a 100 µm thick glass plate with a fabricated antenna. The antenna itself consists of the excitation part, which is either a stripline or another excitation structure (see Section 4.2), and a connecting CPW of matched characteristic impedance (calculated using the TX Line software [46]). The design is then patterned by e-beam lithography into a 1 µm thick PMMA resist coating covered with a conducting layer (Allresist AR-PC 5090), followed by e-beam evaporation of Ti 5 nm/Cu 500 nm/Au 10 nm multilayer, and lift-off. The relatively thick copper layer is used to minimize the ohmic losses due to the approx. 2 cm long connecting CPW length. The fabrication is usually done in batches either on a glass wafer [Fig. 6.2(c)] or on cover glass plates that are consecutively cut into individual units [Fig. 6.2(d)] by a diamond saw dicer.

The second part is a printed circuit board with a CPW providing the interconnection between the SMA connector and the glass cantilever. The glass is glued onto the PCB, and the electrical connection is accomplished by wirebonding, using 25 µm thick and 250 µm wide ribbon wires. The connector is attached to the PCB and soldered, completing the antenna device unit.

This assembly is then fixed onto a manipulator, which besides x-y-z translational motions should favorably have a two-way tilt as well. The tilt manipulator will allow the cantilever to point down against the sample, which can then be lowered into the contact and start flexing. The 100 µm thick glass is conveniently flexible and will withstand bending by at least 2 mm for the 2 cm cantilever length. After the touchdown, we can observe an interference pattern [stripes, demonstrated in Fig. 6.2(e)] that will hint us about a glass tilt present, which can be eliminated by adjusting the tilt angles. Full elimination of the interference pattern is a good indicator that the antenna is in the best achievable contact.

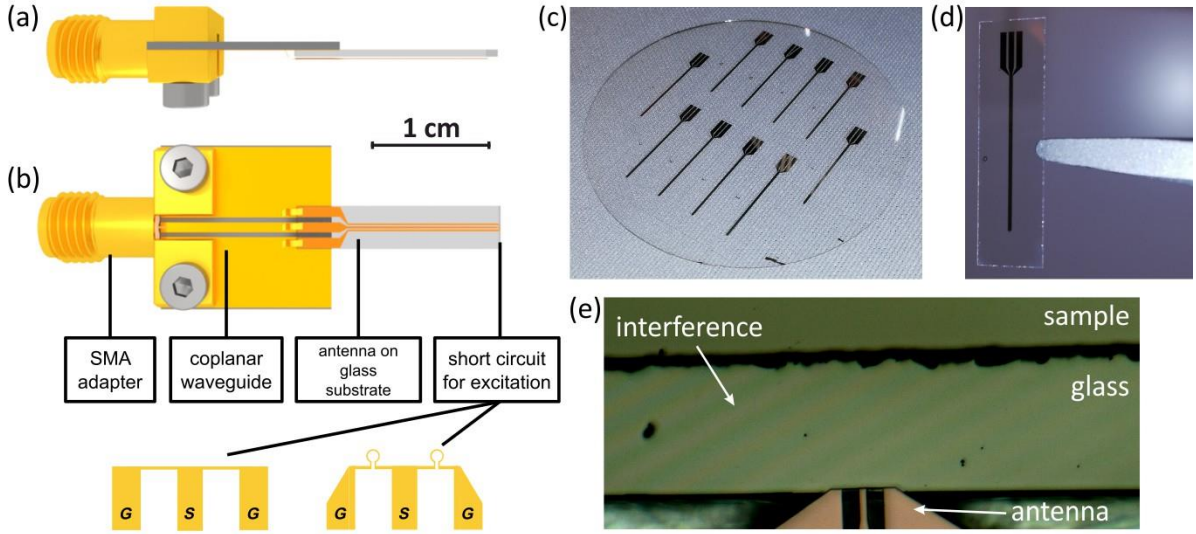

Fig. 6.2: (a) side view and (b) top view of the antenna device with a description of its components. The short-circuiting antenna ending can be modified based on the experimental requirements. The details show the stripline for in-plane excitation and omega-shaped antennas for out-of-plane excitation. Other variants are possible, e.g., a CPW. Reprinted from [54]. *(c) Glass wafer (2") with fabricated antennas. (d) One antenna unit diced from the wafer. (e) Interference pattern of an imperfect antenna landing onto the sample surface. Elimination of the stripes by tilting the stage will result in better contact between the glass cantilever and the sample.*

6.2 Use of the antenna device in BLS experiments

Brillouin light scattering is the typical experimental environment to benefit from the antenna device usage for sample excitation. We have performed a BLS study of the antenna spatial excitation profile on a 240 nm thick CoFeB layer. Fig. 6.3(a,c) shows two graphs mapping the BLS intensity around the stripline ending of the antenna device landed on the layer. The maps show the spin waves propagating in two beams with a significant drop in between them. The intensity drop can be attributed to the excitation phase shift of π between the striplines and thus to the destructive interference of the spin waves between the two antennas.

Fig. 6.3(b,d) shows the intensity dependence in the logarithmic scale along the dotted white lines in (a,c). An exponential fit for the higher field measurement shows a close to linear behavior and allows to determine the decay length of 22.3 µm for the BLS intensity, indicating

a propagating spin-wave mode. For the smaller field, the extraction shows a deviation from a clear linear behavior, indicating a localized, directly excited mode in the antenna's close vicinity. We fit only the points close to the antenna to obtain a decay length for comparison. A value of 11.0 µm is obtained. From the fits, it can be confirmed that the excited mode at 86.3 mT extends further. The different propagation range of both modes can be explained by the spin-wave dispersion relation.

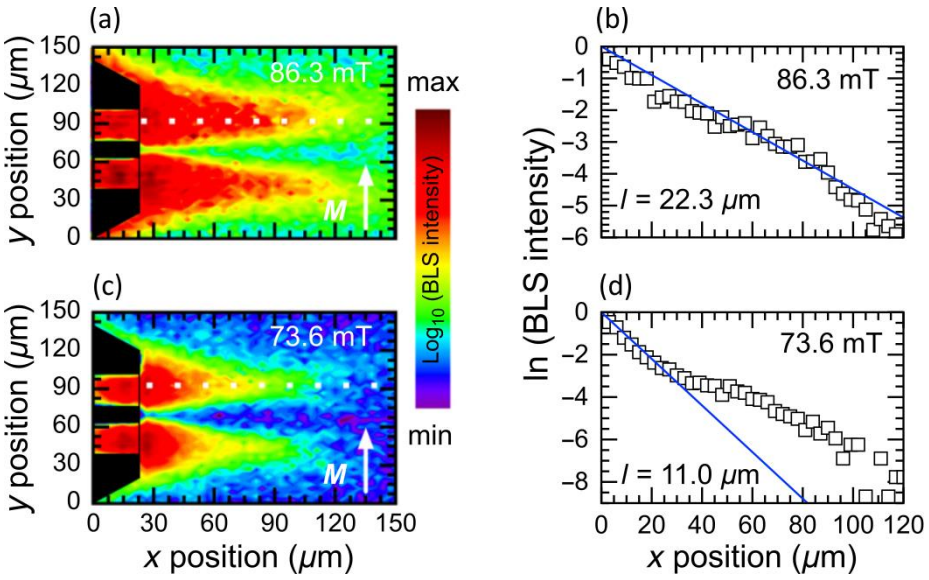

Fig. 6.3: (a,c) 2D maps of BLS intensity at (a) $B = 86.3$ mT and (d) $B = 73.6$ mT. (b,d) shows the BLS intensity plotted along the white dotted lines in (a,c), showing exponential decay. Reprinted from [54].

Conclusion

In the first part of this work, we probed and characterized the magnetic vortex nucleation states using micromagnetic simulations, magnetic imaging by Lorentz microscopy (LTEM), and Magnetic Transmission X-ray Microscopy (MTXM), and we correlated the results with electrical measurements via the anisotropic magnetoresistance (AMR) effect [44]. The advantage of the AMR measurements proved to be in a single disk sensitivity and overall simplicity of the characterization process. However, the pinning and subtle differences between samples proved problematic and made drawing conclusions rather uneasy. We were still able to classify the nucleation process by dividing the nucleation states into the C-state, vortex-pair state, and the buckling state. The characteristic features of the individual states in the AMR curves were also presented, allowing characterization of the nucleation process and, e.g., study the driving effects behind the individual nucleation states with a possibility for statistical studies unattainable by any other method. The acquired knowledge about the vortex nucleation can serve, e.g., for improving the reliability of the vortex switching, which is critical in data storage applications.

The part of this work devoted to vortices was done still at the Faculty of Mechanical Engineering, and later in temporary CEITEC premises in the former FEI company building. But then our moving to new facilities after about two years brought unprecedented experimental options in both sample fabrication (in the new nanofabrication facility) and magnetic characterization (installation of new equipment such as vector network analyzer [VNA],

Brillouin light scattering [BLS], or Kerr microscope), which allowed us for modern magnetization dynamics experiments without the limitations only to the static regime.

The mentioned improvements in our working environment shifted our interests more towards spin-waves [54–56]. We developed experimental processes to measure ferromagnetic resonance (FMR) and propagating spin-wave spectroscopy (PSWS) using the VNA and begun to use the BLS as a great, versatile tool for spin-wave detection. VNA proved to be extremely useful in probing the dynamic material properties, to which the whole Chapter 4 was devoted, describing the VNA basics (receiver operation, sample connection, calibration, excitation in magnetization dynamics experiments), followed by the description of FMR and PSWS experiments from all practical aspects. Chapter 5 then described the developments in the dispersion relation measurement using the PSWS experiment, showing good potential in high quality, detailed results. The dispersion measurements are in good agreement with the dipole-exchange model by Kalinikos and Slavin (presented in Section 1.7), providing room to extract the material parameters by fitting the dispersions.

In the last Chapter 6, we introduced a spin-wave measurement approach using our developed antenna device, discarding the necessity of fabricating the excitation antennas on the sample. The antenna device has a glass cantilever with the excitation antenna, which can be positioned anywhere on the sample. The optical detection using BLS was seamless with a slight decrease of spatial resolution but allowing for more rapid experimental flow. The use of the antenna device in VNA-powered experiments is still mostly opened for development, but electrical measurements' functionality was proven.

References

[1] C. Chappert, A. Fert, F.N. Van Dau, The emergence of spin electronics in data storage., Nat. Mater. 6 (2007) 813–23. https://doi.org/10.1038/nmat2024.

[2] A. Hubert, R. Schäfer, Magnetic Domains - The Analysis of Magnetic Microstructures, Springer, 1998. https://doi.org/10.1007/978-3-540-85054-0.

[3] S.D. Bader, Colloquium: Opportunities in nanomagnetism, Rev. Mod. Phys. 78 (2006) 1. https://doi.org/10.1103/RevModPhys.78.1.

[4] R.P. Cowburn, D.K. Koltsov, A.O. Adeyeye, M.E. Welland, D.M. Tricker, Single-Domain Circular Nanomagnets, Phys. Rev. Lett. 83 (1999) 1042–1045. https://doi.org/10.1103/PhysRevLett.83.1042.

[5] T. Shinjo, T. Okuno, R. Hassdorf, K. Shigeto, T. Ono, Magnetic Vortex Core Observation in Circular Dots of Permalloy, Science (80-.). 289 (2000) 930–932. https://doi.org/10.1126/science.289.5481.930.

[6] S. Wintz, V. Tiberkevich, M. Weigand, J. Raabe, J. Lindner, A. Erbe, A. Slavin, J. Fassbender, Magnetic vortex cores as tunable spin-wave emitters, Nat. Nanotechnol. 11 (2016) 948–953. https://doi.org/10.1038/nnano.2016.117.

[7] A. Mahmoud, F. Ciubotaru, F. Vanderveken, A. V. Chumak, S. Hamdioui, C. Adelmann, S. Cotofana, Introduction to spin wave computing, J. Appl. Phys. 128 (2020) 161101. https://doi.org/10.1063/5.0019328.

[8] T. Kampfrath, A. Sell, G. Klatt, A. Pashkin, S. Mährlein, T. Dekorsy, M. Wolf, M. Fiebig, A. Leitenstorfer, R. Huber, Coherent terahertz control of antiferromagnetic spin waves, Nat. Photonics. 5 (2011) 31–34. https://doi.org/10.1038/nphoton.2010.259.

[9] M. Bailleul, D. Olligs, C. Fermon, S.O. Demokritov, Spin waves propagation and confinement in conducting films at the micrometer scale, Europhys. Lett. 56 (2001) 741–747. https://doi.org/10.1209/epl/i2001-00583-2.

[10] J.M.D. Coey, Magnetism and Magnetic Materials, Cambridge University Press, Cambridge, 2010. https://doi.org/10.1017/CBO9780511845000.

[11] S. Blundell, D. Thouless, Magnetism in Condensed Matter, Oxford University Press, 2003. https://doi.org/10.1119/1.1522704.

[12] O. Wojewoda, Phase–resolved Brillouin light scattering: development and applications, Master's thesis, Faculty of Mechanical Engineering, Brno University of Technology, 2020.

[13] S.-H. Chung, R.D. McMichael, D.T. Pierce, J. Unguris, Phase diagram of magnetic nanodisks measured by scanning electron microscopy with polarization analysis, Phys. Rev. B. 81 (2010) 024410. https://doi.org/10.1103/PhysRevB.81.024410.

[14] L. Landau, E. Lifshits, on the Theory of the Dispersion of Magnetic Permeability in Ferromagnetic Bodies, Phys. Zeitsch. Der Sow. 169 (1935) 14–22.

[15] T.L. Gilbert, Classics in Magnetics A Phenomenological Theory of Damping in Ferromagnetic Materials, IEEE Trans. Magn. 40 (2004) 3443–3449. https://doi.org/10.1109/TMAG.2004.836740.

[16] B. Hillebrands, K. Ounadjela, Spin dynamics in confined magnetic structures I, Springer, 2002. https://doi.org/10.1007/3-540-40907-6.

[17] C. Kittel, On the Theory of Ferromagnetic Resonance Absorption, Phys. Rev. 73 (1948) 155–161. https://doi.org/10.1103/PhysRev.73.155.

[18] C. Herring, C. Kittel, On the Theory of Spin Waves in Ferromagnetic Media, Phys. Rev. 81 (1951) 869–880. https://doi.org/10.1103/PhysRev.81.869.

[19] R.W. Damon, J.R. Eshbach, Magnetostatic Modes of a Ferromagnetic Slab, J. Appl. Phys. 31 (1960) S104–S105. https://doi.org/10.1063/1.1984622.

[20] T. Schneider, A.A. Serga, T. Neumann, B. Hillebrands, M.P. Kostylev, Phase reciprocity of spin-wave excitation by a microstrip antenna, Phys. Rev. B - Condens. Matter Mater. Phys. 77 (2008) 214411. https://doi.org/10.1103/PhysRevB.77.214411.

[21] K. Sekiguchi, K. Yamada, S.M. Seo, K.J. Lee, D. Chiba, K. Kobayashi, T. Ono, Nonreciprocal emission of spin-wave packet in FeNi film, Appl. Phys. Lett. 97 (2010) 022508. https://doi.org/10.1063/1.3464569.

[22] L. Flajšman, Magneto-optical study of the dynamic properties of magnetic nanostructures and nanostructured metamaterials, Doctoral thesis, Central European Institute of Technology, Brno University of Technology, 2019.

[23] B.A. Kalinikos, A.N. Slavin, Theory of dipole-exchange spin wave spectrum for ferromagnetic films with mixed exchange boundary conditions, J. Phys. C Solid State Phys. 19 (1986) 7013–7033. https://doi.org/10.1088/0022-3719/19/35/014.

[24] A. Kreisel, F. Sauli, L. Bartosch, P. Kopietz, Microscopic spin-wave theory for yttrium-iron garnet films, Eur. Phys. J. B. 71 (2009) 59–68. https://doi.org/10.1140/epjb/e2009-00279-y.

[25] J.N. Chapman, The investigation of magnetic domain structures in thin foils by electron microscopy, J. Phys. D. Appl. Phys. 17 (1984) 623–647. https://doi.org/10.1088/0022-3727/17/4/003.

[26] M. De Graef, Y. Zhu, Magnetic imaging and its applications to materials, Academic Press, 2001.

[27] D.T. Ngo, L.T. Kuhn, In situ transmission electron microscopy for magnetic nanostructures, Adv. Nat. Sci. Nanosci. Nanotechnol. 7 (2016) 045001. https://doi.org/10.1088/2043-6262/7/4/045001.

[28] C. Phatak, M. Tanase, A.K. Petford-Long, M. De Graef, Determination of magnetic vortex polarity from a single Lorentz Fresnel image, Ultramicroscopy. 109 (2009) 264–267. https://doi.org/10.1016/j.ultramic.2008.11.003.

[29] S.K. Walton, K. Zeissler, W.R. Branford, S. Felton, MALTS: A Tool to Simulate Lorentz Transmission Electron Microscopy From Micromagnetic Simulations, IEEE Trans. Magn. 49 (2013) 4795–4800. https://doi.org/10.1109/TMAG.2013.2247410.

[30] H. Hopster, H.P. Oepen, eds., Magnetic Microscopy of Nanostructures, Springer Berlin Heidelberg, Berlin, Heidelberg, 2005. https://doi.org/10.1007/b137837.

[31] P. Fischer, D.-H. Kim, W. Chao, J.A. Liddle, E.H. Anderson, D.T. Attwood, Soft X-ray microscopy of nanomagnetism, Mater. Today. 9 (2006) 26–33. https://doi.org/10.1016/S1369-7021(05)71335-3.

[32] P. Fischer, Viewing spin structures with soft X-ray microscopy, Mater. Today. 13 (2010) 14–22. https://doi.org/10.1016/S1369-7021(10)70161-9.

[33] J. Thieme, G. Schmahl, D. Rudolph, E. Umbach, eds., X-Ray Microscopy and Spectromicroscopy, Springer Berlin Heidelberg, 1998. https://doi.org/10.1007/978-3-642-72106-9.

[34] D.T. Attwood, Soft X-rays and Extreme Ultraviolet Radiation: Principles and Applications, Cambridge University Press, 1999. https://doi.org/10.1017/CBO9781107477629.

[35] T. McGuire, R. Potter, Anisotropic magnetoresistance in ferromagnetic 3d alloys, IEEE Trans. Magn. 11 (1975) 1018–1038. https://doi.org/10.1109/TMAG.1975.1058782.

[36] M.N. Baibich, J.M. Broto, A. Fert, F.N. Van Dau, F. Petroff, P. Etienne, G. Creuzet, A. Friederich, J. Chazelas, Giant Magnetoresistance of (001)Fe/(001)Cr Magnetic Superlattices, Phys. Rev. Lett. 61 (1988) 2472–2475. https://doi.org/10.1103/PhysRevLett.61.2472.

[37] T. Miyazaki, N. Tezuka, Giant magnetic tunneling effect in Fe/Al2O3/Fe junction, J. Magn. Magn. Mater. 139 (1995) L231–L234. https://doi.org/10.1016/0304-8853(95)90001-2.

[38] M. Vaňatka, Magnetic multilayers for spintronics applications, Bachelor's thesis, Faculety of Mechanical Engineering, Brno University of Technology, 2013.

[39] K. Guslienko, V. Novosad, Y. Otani, H. Shima, K. Fukamichi, Magnetization reversal due to vortex nucleation, displacement, and annihilation in submicron ferromagnetic dot arrays, Phys. Rev. B. 65 (2001) 024414. https://doi.org/10.1103/PhysRevB.65.024414.

[40] K.S. Buchanan, P.E. Roy, M. Grimsditch, F.Y. Fradin, K.Y. Guslienko, S.D. Bader, V. Novosad, Soliton-

pair dynamics in patterned ferromagnetic ellipses, Nat. Phys. 1 (2005) 172–176. https://doi.org/10.1038/nphys173.

[41] M. Rahm, M. Schneider, J. Biberger, R. Pulwey, J. Zweck, D. Weiss, Vortex nucleation in submicrometer ferromagnetic disks, Appl. Phys. Lett. 82 (2003) 4110–4112. https://doi.org/10.1063/1.1581363.

[42] S.R. Bakaul, B.L. Wu, G.C. Han, Y.H. Wu, Probing magnetization reversal process in ferromagnetic disk by superconductor-ferromagnet junction, Appl. Phys. Lett. 97 (2010) 1–3. https://doi.org/10.1063/1.3463474.

[43] T. Wren, O. Kazakova, Anisotropic magnetoresistance effect in sub-micron nickel disks, J. Appl. Phys. 117 (2015) 17E134. https://doi.org/10.1063/1.4918967.

[44] M. Vaňatka, M. Urbánek, R. Jíra, L. Flajšman, M. Dhankhar, M.-Y. Im, J. Michalička, V. Uhlíř, T. Šikola, Magnetic vortex nucleation modes in static magnetic fields, AIP Adv. 7 (2017) 105103. https://doi.org/10.1063/1.5006235.

[45] M. Hiebel, Fundamentals of vector network analysis, Rohde & Schwarz, 2016.

[46] TX-LINE: A free and interactive calculator for the analysis and synthesis of transmission-line structures available for free from AWR Software, (n.d.). https://www.awr.com/awr-software/options/tx-line.

[47] V. Vlaminck, M. Bailleul, Spin-wave transduction at the submicrometer scale: Experiment and modeling, Phys. Rev. B. 81 (2010) 014425. https://doi.org/10.1103/PhysRevB.81.014425.

[48] I.S. Maksymov, M. Kostylev, Broadband stripline ferromagnetic resonance spectroscopy of ferromagnetic films, multilayers and nanostructures, Phys. E Low-Dimensional Syst. Nanostructures. 69 (2015) 253–293. https://doi.org/10.1016/J.PHYSE.2014.12.027.

[49] H. Yu, O. D'Allivy Kelly, V. Cros, R. Bernard, P. Bortolotti, A. Anane, F. Brandl, R. Huber, I. Stasinopoulos, D. Grundler, Magnetic thin-film insulator with ultra-low spin wave damping for coherent nanomagnonics, Sci. Rep. 4 (2014) 1–5. https://doi.org/10.1038/srep06848.

[50] J. Chen, F. Heimbach, T. Liu, H. Yu, C. Liu, H. Chang, T. Stückler, J. Hu, L. Zeng, Y. Zhang, Z. Liao, D. Yu, W. Zhao, M. Wu, Spin wave propagation in perpendicularly magnetized nm-thick yttrium iron garnet films, J. Magn. Magn. Mater. 450 (2018) 3–6. https://doi.org/10.1016/j.jmmm.2017.04.045.

[51] H. Qin, S.J. Hämäläinen, K. Arjas, J. Witteveen, S. van Dijken, Propagating spin waves in nanometer-thick yttrium iron garnet films: Dependence on wave vector, magnetic field strength, and angle, Phys. Rev. B. 98 (2018) 224422. https://doi.org/10.1103/PhysRevB.98.224422.

[52] Y. V. Khivintsev, Y.A. Filimonov, S.A. Nikitov, Spin wave excitation in yttrium iron garnet films with micron-sized antennas, Appl. Phys. Lett. 106 (2015) 052407. https://doi.org/10.1063/1.4907626.

[53] S.A. Nikitov, D. V Kalyabin, I. V Lisenkov, A. Slavin, Y.N. Barabanenkov, S.A. Osokin, A. V Sadovnikov, E.N. Beginin, M.A. Morozova, Y.A. Filimonov, Y. V Khivintsev, S.L. Vysotsky, V.K. Sakharov, E.S. Pavlov, Magnonics: a new research area in spintronics and spin wave electronics, Physics-Uspekhi. 58 (2015) 1002–1028. https://doi.org/10.3367/ufne.0185.201510m.1099.

[54] T. Hache, M. Vaňatka, L. Flajšman, T. Weinhold, T. Hula, O. Ciubotariu, M. Albrecht, B. Arkook, I. Barsukov, L. Fallarino, O. Hellwig, J. Fassbender, M. Urbánek, H. Schultheiss, Freestanding Positionable Microwave-Antenna Device for Magneto-Optical Spectroscopy Experiments, Phys. Rev. Appl. 13 (2020) 054009. https://doi.org/10.1103/PhysRevApplied.13.054009.

[55] L. Flajšman, K. Wagner, M. Vaňatka, J. Gloss, V. KřiŽáková, M. Schmid, H. Schultheiss, M. Urbánek, Zero-field propagation of spin waves in waveguides prepared by focused ion beam direct writing, Phys. Rev. B. 101 (2020) 014436. https://doi.org/10.1103/PhysRevB.101.014436.

[56] O. Wojewoda, T. Hula, L. Flajšman, M. Vaňatka, J. Gloss, J. Holobrádek, M. Staňo, S. Stienen, L. Körber, K. Schultheiss, M. Schmid, H. Schultheiss, M. Urbánek, Propagation of spin waves through a Néel domain wall, Appl. Phys. Lett. 117 (2020) 022405. https://doi.org/10.1063/5.0013692.